

HMGA2 and protein leucine methylation drive pancreatic cancer lineage plasticity

Received: 28 August 2024

Accepted: 14 May 2025

Published online: 26 May 2025

 Check for updates

Stephanie Dobersch¹, Naomi Yamamoto^{1,2,3}, Aidan Schutter¹, Sarah M. Cavender¹, Tess M. Robertson¹, Nithya Kartha¹, Annie N. Samraj⁴, Ben Doron¹, Lisa A. Poole¹, Cynthia L. Wladyka¹, Amy Zhang⁵, Gun Ho Jang⁵, Aswanth H. Mahalingam⁶, Guillermo Barreto^{7,8}, Srivatsan Raghavan^{6,9,10,11}, Goutham Narla^{12,13}, Faiyaz Notta^{5,14,15}, Robert N. Eisenman¹⁶, Andrew C. Hsieh^{1,17,18} & Sita Kugel^{1,18} ✉

Basal pancreatic ductal adenocarcinoma (PDAC) has the worst overall survival and is the only subtype that serves as an independent poor prognostic factor. We identify elevated levels of LIN28B and its downstream target, HMGA2, in basal PDAC. Notably, LIN28B significantly accelerates KRAS-driven PDAC progression in a mouse model. Here, we show that HMGA2 promotes basal PDAC pathogenesis by enhancing mRNA translation downstream of LIN28B. Mechanistically, HMGA2 suppresses leucine carboxyl methyltransferase 1 (LCMT1) at the chromatin level, reducing PP2A methylation and activity. This leads to increased phosphorylation of S6K and eIF4B, boosting mRNA translation. Additionally, HMGA2 downregulates B56 α (PPP2R5A), disrupting functional PP2A holoenzyme assembly and further sustaining phosphorylated S6K levels. Impaired PP2A function mimics HMGA2's effects, reinforcing increased mRNA translation and basal lineage features. This work uncovers a critical link between the LIN28B/HMGA2 axis, protein synthesis, and PDAC lineage specificity via LCMT1-mediated PP2A methylation and B56 α -PP2A disruption.

Pancreatic ductal adenocarcinoma (PDAC) is one of the most lethal human malignancies, responsible for 466,003 deaths worldwide in 2020. It is projected to become the second leading cause of cancer deaths in the United States by 2030¹. Combination chemotherapy with FOLFIRINOX (FFOX) or nab-paclitaxel plus gemcitabine (GnP) is the

preferred first-line treatment for patients with metastatic PDAC², which continues to carry a prognosis of less than one year. Most PDAC tumors host a similar suite of genetic mutations, including *KRAS*, *TP53*, *CDKN2A*, and *SMAD4*. These mutations are acquired sequentially through precursor lesions called pancreatic intraepithelial neoplasias

¹Human Biology Division, Fred Hutchinson Cancer Center, Seattle, WA, USA. ²Medical Scientist Training Program, University of Washington, Seattle, WA, USA. ³Molecular & Cellular Biology Graduate Program, University of Washington, Seattle, WA, USA. ⁴Division of Transfusion Medicine, Department of Laboratory Medicine, University of Washington School of Medicine, Seattle, WA, USA. ⁵PanCuRx Translational Research Initiative, Ontario Institute for Cancer Research, Toronto, Ontario, Canada. ⁶Department of Medical Oncology, Dana-Farber Cancer Institute, Boston, MA, USA. ⁷Université de Lorraine, CNRS, Laboratoire IMoPA, Nancy, France. ⁸Lung Cancer Epigenetic, Max-Planck-Institute for Heart and Lung Research, Bad Nauheim, Germany. ⁹Broad Institute of MIT and Harvard, Cambridge, MA, USA. ¹⁰Harvard Medical School, Boston, MA, USA. ¹¹Department of Medicine, Brigham and Women's Hospital, Boston, MA, USA. ¹²Division of Genetic Medicine, Department of Internal Medicine, University of Michigan, Ann Arbor, MI, USA. ¹³Rogel Cancer Center, University of Michigan, Ann Arbor, MI, USA. ¹⁴Princess Margaret Cancer Centre, University Health Network, Toronto, ON, Canada. ¹⁵Department of Medical Biophysics, University of Toronto, Toronto, ON, Canada. ¹⁶Basic Sciences Division, Fred Hutchinson Cancer Center, Seattle, WA, USA. ¹⁷Department of Medicine, University of Washington, Seattle, WA, USA. ¹⁸Department of Genome Sciences, University of Washington, Seattle, WA, USA. ✉e-mail: skugel@fredhutch.org

(PanINs), which were recently demonstrated to be both multifocal and widespread in normal pancreas³. Genetically engineered mouse models (GEMMs) have faithfully recapitulated this sequence of genetic aberrations but still do not model specific pathologic or molecular subtypes of PDAC. We know that pancreatic cancer is phenotypically complex, given that patients exhibit very heterogeneous responses to chemotherapy. To understand these differences, researchers have characterized the transcriptional profiles of PDACs. This work led to the discovery that there are two distinct subtypes of pancreatic cancer: classical and basal. Basal PDAC is more aggressive and has poorer overall survival⁴. Understanding what defines each subtype, their susceptibilities, and mechanisms of resistance will help to identify new targeted therapies and lead to more treatment options for this devastating disease.

LIN28A and B are highly conserved RNA-binding proteins that are strongly expressed in embryonic stem cells, lose expression with differentiation⁵, and can substitute for MYC in the Yamanaka factors, thus demonstrating their important role in establishing a pluripotent state^{6,7}. Both LIN28 isoforms have been well characterized as degraders of microRNAs (miRNAs), specifically the *let-7* family^{8–12}. While LIN28A is predominately cytoplasmic and requires TUTase activity to block Dicer processing of *let-7* miRNAs, LIN28B is found in the nucleus and its role in regulating *let-7* degradation is TUT-independent¹³. By suppressing maturation of *let-7* miRNAs, high expression of LIN28A or LIN28B leads to de-repression of *let-7* targets. These targets allow for de-differentiation of adult cells, thus the LIN28/*let-7* axis is crucial in regulating cell growth, homeostasis, and replicative potential^{5,12,14–19}. In embryonic tissues, LIN28 levels are high and *let-7* is suppressed, allowing for increased metabolism, proliferation, and growth. In normal adult tissues, LIN28 is silenced and thus *let-7* is high^{5,12,14}, but a variety of cancers have been shown to reactivate LIN28A or LIN28B^{19–21}. Prior studies have demonstrated that upregulation of either LIN28 isoform is typically exclusive of the other isoform and that the isoform expressed correlates with cancer subtype¹³. We have previously found that LIN28B is highly expressed in a subset of human PDAC²². LIN28B expression is correlated with advanced disease and poor prognosis across cancer types^{20,23,24}. The most well-characterized downstream targets of LIN28B are insulin growth factor 2 binding proteins (IGFBPs, also known as IMPs) and high-mobility group (HMG) protein AT-hook 2 (HMGA2)^{17,25–27}. High expression of IMP1, IMP3, and HMGA2 is associated with increased aggressiveness and metastasis in PDAC^{28,29}. Importantly, LIN28B was found to be highly expressed in circulating tumor cells from PDAC patients, and expression was prognostic for a worse overall survival³⁰.

Here, we define how LIN28B and its downstream target, HMGA2, drive the basal subtype of PDAC. We show that the expression of the LIN28B/HMGA2 axis promotes a more aggressive disease phenotype in vitro and in vivo. Furthermore, we demonstrate that HMGA2 orchestrates the pathogenesis of basal PDAC by reducing leucine methylation of PP2A, thereby inhibiting its activity on a critical node of the mRNA translation machinery. This finding reveals a vulnerability of basal PDAC to protein synthesis inhibition, representing a promising subtype-specific therapeutic target.

Results

LIN28B accelerates for tumor initiation and progression in vitro and in vivo

To study the role of LIN28B in PDAC initiation and maintenance, we generated a GEMM incorporating a conditional, doxycycline (dox)-inducible, human *FLAG-LIN28B*³¹ into the background of *Kras^{LSL-G12D};p48Cre* (KC) mice to generate *Kras^{LSL-G12D};LIN28B^{LSL-Dox};p48Cre* (K28C) animals. K28C mice treated for 15 days with 200 µg/ml doxycycline showed sporadic expression of FLAG-LIN28B in the exocrine pancreas (Supplementary Fig. 1a). After 15 weeks of doxycycline treatment, FLAG-LIN28B

was highly expressed in ductal cells in K28C pancreata (Supplementary Fig. 1b). Remarkably, in the context of mutant KRAS expression in the pancreas, activation of LIN28B significantly accelerated the progression of lethal pancreatic tumors. K28C animals exhibited a median survival of 45 weeks, substantially shorter than dox-treated KC animals, which had a median survival of 88 weeks (Fig. 1a). Given that our model does not genetically perturb p53, unlike the most common GEMMs of PDAC^{32,33}, we explored levels of p53 in tumors between K28C, KC, *KP^{+/−}C*, and *KP^{−/−}C* animals. At disease endpoint, both K28C and KC tumors exhibited nuclear expression of p53 at similar levels to *KP^{+/−}C* tumors, suggesting that our tumor model requires impaired p53 function but not complete loss (Supplementary Fig. 1c–d). LIN28B expression alone did not result in tumor formation after two years (Fig. 1a). To confirm earlier onset of PDAC in K28C mice, we harvested cohorts of KC and K28C animals at 5-, 10-, and 15-weeks after beginning dox treatment (Supplementary Fig. 1e). At the 5 week time point, high-grade PanINs and PDAC were increased in K28C animals compared to KC animals (Fig. 1b). At 30 weeks, K28C primary tumors displayed the invasive gland formation and associated desmoplastic stromal response typical of pancreatic cancer (Fig. 1c). Metastases to lung and liver were observed in both K28C and KC models at endpoint (median 45 weeks in K28C and 88 weeks in KC, Fig. 1c). Importantly, these results demonstrate that LIN28B accelerates both the formation and metastatic spread of KrasG12D-driven PDAC. Even though LIN28B expression alone did not lead to tumor formation in vivo, we found a dramatic increase in the ability of pancreatic ductal cells isolated from the pancreata of 28C mice to form organoids compared with Cre alone (C), suggesting expression of LIN28B could increase tumor initiating capacity (Supplementary Fig. 1f–g). Notably, 28C organoids isolated from normal pancreas expressed higher levels of p53 compared to organoids isolated from tumors (K28C, KC and *KP^{+/−}C*, Supplementary Fig. 1h). LIN28B-expressing pancreata from 28C mice showed no histological abnormalities compared to mice expressing only Cre (Supplemental Fig. 1e). Thus, LIN28B is not sufficient alone but can cooperate with oncogenic KRAS to accelerate PDAC and is necessary for tumor progression.

Our data support the concept that LIN28B expression cooperates with oncogenic KRAS to accelerate PDAC in vivo. Building upon this observation, we were motivated to determine if LIN28B played a role in tumor maintenance as well as tumor initiation. We removed dox water from a cohort of mice following 5 weeks initial dox exposure, leading to loss of LIN28B expression. At 5 weeks, high-grade PanINs and PDAC are present in K28C mice (Fig. 1b, Supplementary Fig. 1e). Our results showed that early withdrawal of LIN28B substantially increased the survival of K28C mice, prolonging median survival to similar time-points as seen in KC mice (Fig. 1e). In addition to improving survival, dox withdrawal in K28C mice led to less aggressive disease, with most mice requiring euthanasia due to pancreatic cyst formation and displaying a foamy gland phenotype upon histological examination, in contrast to mice with continual dox exposure (Fig. 1e–f). This phenotype resembles a rare variant of PDAC in humans that can be misdiagnosed as a benign lesion and is notable for foamy-appearing cytoplasm and basally compressed nuclei^{34,35}. Thus, we conclude that continuous expression of LIN28B is necessary for the aggressive disease phenotype we observe in our K28C mouse model, and that LIN28B expression contributes not only to tumor initiation but also continued accelerated growth and metastasis when combined with oncogenic KRAS.

HMGA2 regulates tumor growth in vitro and in vivo downstream of LIN28B

To determine what downstream target of LIN28B mediates PDAC growth and survival in vivo, we turned to the well-characterized

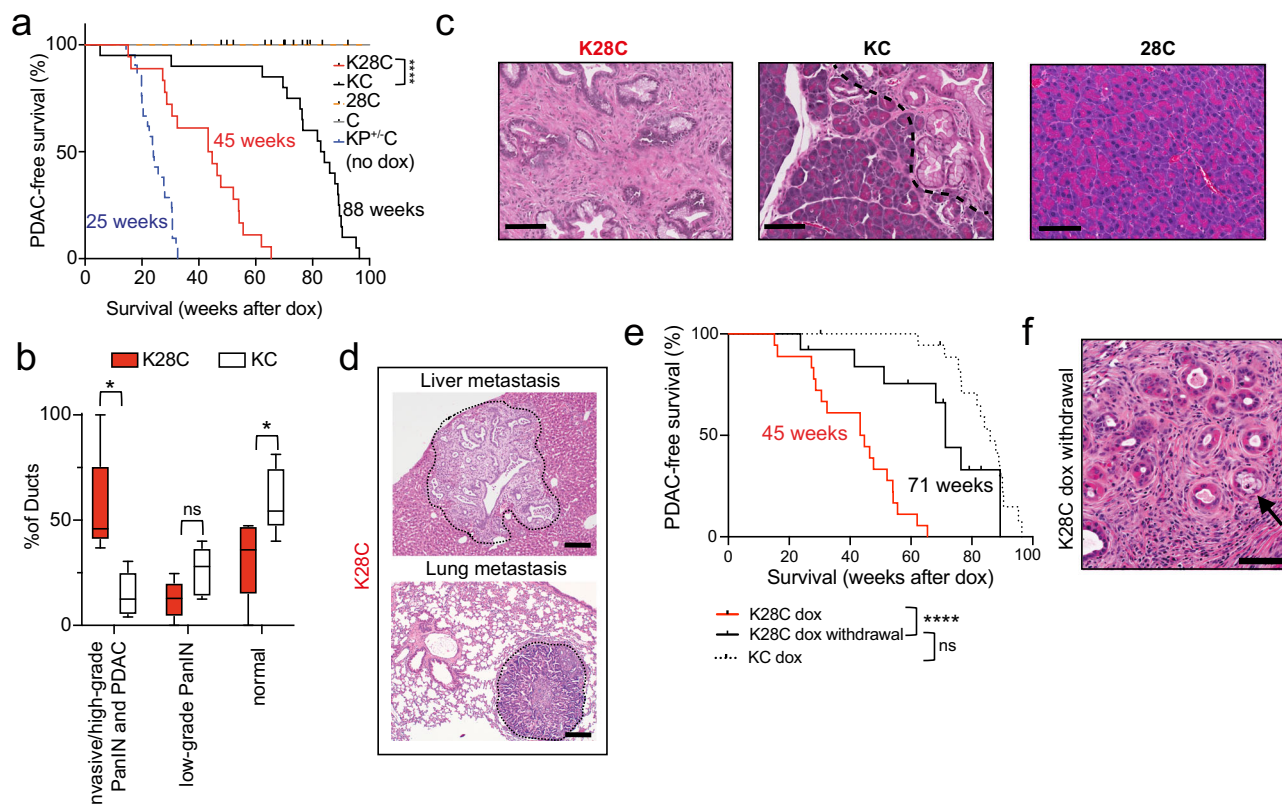


Fig. 1 | LIN28B accelerates tumor initiation and progression in vitro and in vivo.

a PDAC-free survival analysis of GEMMs. KP^{+/-}C model (KrasG12D, p53^{+/-}, p48-Cre) provided for comparison. All mice except the KP^{+/-}C model were continuously treated with doxycycline. K28C: KrasLSL-G12D, LIN28BLSL-Dox, p48Cre; KC: KrasLSL-G12D, p48Cre; 28C: LIN28BLSL-Dox, p48Cre; C: p48Cre. N(K28C) = 18 mice, n(KC) = 20 mice, n(28C) = 15 mice, n(C) = 12 mice and n(KP^{+/-}C) = 21 mice; asterisks, *P* values after log-rank test. *****P* < 0.0001 K28C vs KC. **b** Percentage of invasive/high-grade PanIN and PDAC, low grade PanIN, and normal ducts in 5-week-old K28C and KC mice. Box plots represent median, interquartile range, and 5–95th percentile of *n* = 5 mice. Asterisks, *P* values after unpaired, two-tailed *t* test. **P* = 0.0102 K28C vs KC, invasive/high-grade; **P* = 0.038 K28C vs KC, normal; ns, non-significant. **c** Representative H&E stains of PDAC in 30-week-old K28C (entirely PDAC), KC (PanIN and normal pancreas separated by dashed line), and 28C mice (entirely normal pancreas). Scale bar = 100 μm. **d** Representative H&E stains of liver and lung metastases in K28C mice. Dotted line indicates border of metastatic foci. Scale bars = 100 μm. **e** PDAC-free survival analysis of GEMMs withdrawn from doxycycline (dox) after 5 weeks. GEMMs treated with doxycycline were added for comparison and are the same as in Fig. 1a. N(K28C dox withdrawal) = 13 mice; asterisks, *P* values after log-rank test. *****P* < 0.0001 K28C dox withdrawal vs K28C dox; ns, non-significant. **f** Representative H&E staining of PDAC in K28C dox withdrawal mice at endpoint. Arrow shows foamy cell phenotype. Scale bar, 100 μm. Source data are provided as a Source Data file.

non-significant. **c** Representative H&E stains of PDAC in 30-week-old K28C (entirely PDAC), KC (PanIN and normal pancreas separated by dashed line), and 28C mice (entirely normal pancreas). Scale bar = 100 μm. **d** Representative H&E stains of liver and lung metastases in K28C mice. Dotted line indicates border of metastatic foci. Scale bars = 100 μm. **e** PDAC-free survival analysis of GEMMs withdrawn from doxycycline (dox) after 5 weeks. GEMMs treated with doxycycline were added for comparison and are the same as in Fig. 1a. N(K28C dox withdrawal) = 13 mice; asterisks, *P* values after log-rank test. *****P* < 0.0001 K28C dox withdrawal vs K28C dox; ns, non-significant. **f** Representative H&E staining of PDAC in K28C dox withdrawal mice at endpoint. Arrow shows foamy cell phenotype. Scale bar, 100 μm. Source data are provided as a Source Data file.

transcripts targeted by *let-7*. *Let-7* miRNAs promote the degradation of multiple transcripts involved in carcinogenesis^{16–18}, and are inhibited by LIN28B^{8–12}. Gene set enrichment analysis (GSEA) comparing PDAC tumors^{36–40} and cell lines⁴¹ with high versus low expression of LIN28B revealed that LIN28B^{high} tumors were strongly enriched for the expression of *let-7* targets, curated in two independent gene sets. While we and others have demonstrated that LIN28B promotes cellular transformation through the inhibition of *let-7* tumor suppressive microRNAs^{13,21,22}, it remains unclear why LIN28B is required for the continued growth of established cancer cells, particularly in the presence of activated KRAS.

We verified that withdrawal of dox from K28C murine tumor cells led to rapid loss of LIN28B expression, a concomitant rise in *let-7* levels, and reduction of HMGA2, IMP1, and IMP3 (Fig. 2a–b). HMGA2 is a well-established direct target of *let-7*, with eight binding sites in its 3' UTR, and has itself been implicated as a potential oncogene when upregulated⁴². In our LIN28B^{high} human and murine basal PDAC cell lines, knockdown of *HMGA2* led to a dramatic reduction in cell growth, mirroring the growth defects seen with *LIN28B* knockdown²² (Fig. 2c–d, Supplementary Fig. 2a–b). Moreover, overexpression of an *HMGA2* construct lacking a 3' UTR rescued the growth defect after *LIN28B* knockdown (Fig. 2e, Supplementary Fig. 2c). These data suggest that downstream of LIN28B, HMGA2 is necessary and sufficient for oncogenic proliferation in PDAC.

LIN28B/HMGA2 expression is high in basal PDAC

HMGA2 is an architectural transcription factor that interacts with various other transcription factors (such as NF-κappaB p50, SMAD3) and can enhance or repress gene transcription depending on the context^{43–46}. HMGA2 is also involved in regulating cell growth, differentiation, and development, and its dysregulation has been linked to cancer progression in multiple tissues⁴⁷. HMGA2 is recognized for its interactions with critical signaling pathways, including the transforming growth factor-beta (TGF-β) signaling pathway. Studies have shown that HMGA2 can modulate TGF-β signaling by acting as a downstream target or interacting directly with components of the pathway. HMGA2 has been reported to enhance TGF-β-induced signaling, promoting processes such as epithelial–mesenchymal transition (EMT), and fibrosis^{48,49}. Previous studies have proposed that HMGA2 plays no role in PDAC progression in KP^{+/-}C and KP^{-/-}C GEMMs⁵⁰, but our data suggest that HMGA2 is necessary for a subset of cancer cells to sustain oncogenic growth. To further elucidate the importance of the LIN28B/HMGA2 axis, we used western blotting to assess protein expression of these two targets in various human PDAC cell lines and organoids. Notably, we found that both LIN28B and HMGA2 expression were significantly increased in the basal PDAC subtype (Fig. 3a–b, Supplementary Fig. 3a). Furthermore, RNAseq of laser-capture microdissected patient biopsies showed significantly higher levels of *HMGA2* in the basal/quasi-mesenchymal/squamous subtype across multiple

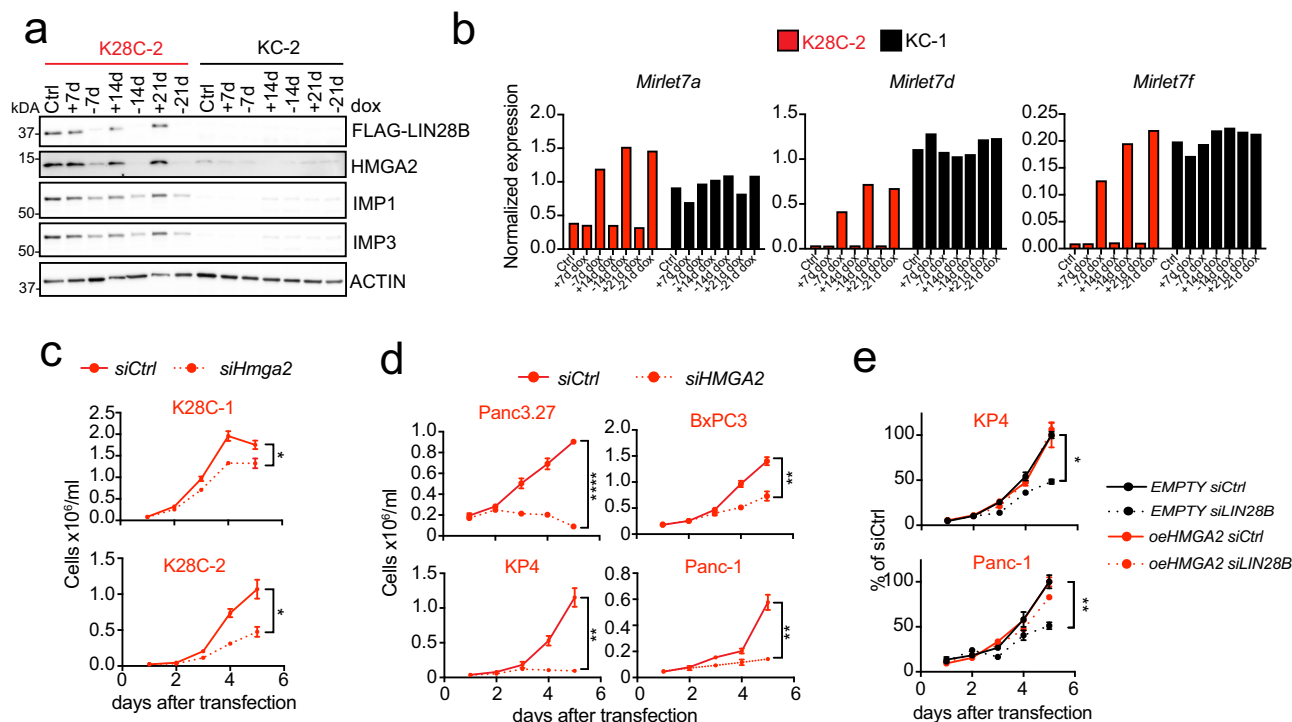


Fig. 2 | HMG2 regulates tumor growth in vitro and in vivo downstream of LIN28B. **a–b**, Expression of FLAG-LIN28B, HMG2, IMP1, IMP3, and ACTIN by Western Blot (WB) (**a**) and *let-7a/d/f* miRNAs by qRT-PCR (**b**) in K28C and KC murine PDAC cell lines with and without doxycycline treatment for 7, 14, and 21 days. Data are displayed as means of technical duplicates. **c–d**, Growth curves of murine (**c**) or human basal (**d**) PDAC cell lines transfected with siRNA against *HMG2* or a non-targeting control. Data are displayed as means \pm s.e.m ($n = 3$ biologically independent experiments); asterisks, P values after unpaired, two-tailed t test. * $P = 0.0453$ siHmg2 vs siCtrl, K28C-1; * $P = 0.0161$ siHmg2 vs siCtrl, K28C-2;

**** $P < 0.0001$ siHMG2 vs siCtrl, Panc3.27; ** $P = 0.0014$ siHMG2 vs siCtrl, KP4; ** $P = 0.0048$ siHMG2 vs siCtrl, BxPC3; ** $P = 0.0020$ siHMG2 vs siCtrl, Panc-1. **e** Growth curves of human basal PDAC cell lines engineered to overexpress HMG2 or empty vector upon doxycycline treatment. Cells were transfected with siRNA against *LIN28B* or a non-targeting control. Data are displayed as means \pm s.e.m ($n = 3$ biologically independent experiments); asterisks, P values after unpaired, two-tailed t test. * $P = 0.0150$ day 5 EMPTY+siCtrl vs EMPTY+siLIN28B, KP4; ** $P = 0.0041$ day 5 EMPTY+siCtrl vs EMPTY+siLIN28B, Panc-1; ns, non-significant. Source data are provided as a Source Data file.

subtyping algorithms and in both localized and metastatic tumors compared to the classical subtype (Fig. 3c)^{51,52}. These findings were replicated using an independent dataset of 21 metastatic patient biopsies, where *HMG2* expression was higher in the basal subtype and overlapped with expression of *KRT5*, *KRT7*, *KRT17*, *KRT81*, and *TP63*, known markers of basal PDAC (Supplementary Fig. 3b)^{53–58}. Finally, a human organoid induced to a more basal subtype through treatment with TGF- β displayed increased *HMG2* expression (Supplementary Fig. 3c).

Next, we sought to determine if expression of *HMG2* in classical PDAC cell lines was sufficient to convert cells to a basal subtype. We engineered classical cell lines to overexpress a dox-inducible wild-type (WT) *HMG2* construct, then titrated dox to achieve *HMG2* levels to those in basal PDAC (Supplementary Fig. 3d). Overexpression of WT *HMG2* in classical lines dramatically increased the expression of several basal markers (*KRT5*, *KRT17*, *KRT81*) in vitro (Fig. 3d) and when grown as an orthotopic xenograft (Fig. 3e–f). Given the clear association of *HMG2* and the basal subtype in human disease, we were curious whether our K28C model was more basal than KC littermates. We performed immunohistochemistry (IHC) for basal (*KRT5*) and classical (*GATA6*) markers^{54–57,59–62} in 5 and 30-week-old K28C and KC mice and observed a substantial increase in basal markers only in K28C tumors, which mirrored *HMG2* expression (Fig. 3g–i). Therefore, we have established *HMG2* as a strong marker for the basal subtype in both human and murine PDAC and have developed a disease-relevant GEMM of basal PDAC. These data demonstrate that *HMG2* can control PDAC lineage, driving cells toward an aggressive basal subtype.

HMG2 drives proliferation through upregulation of S6K and mRNA translation independent of mTOR in basal PDAC

Given the dramatic effect of *HMG2* knockdown on the growth of *HMG2*^{high} PDAC, we hypothesized that *HMG2* regulates pro-growth pathways. We knocked down *HMG2* in three basal *HMG2*^{high} human cell lines and conducted a candidate gene analysis of major drivers of growth. Interestingly, growth did not appear to be driven by ERK, AKT, or mTOR but rather a downstream mTOR target, S6K (Fig. 4a, Supplementary Fig. 4a–b). The mTOR pathway is critical for cancer initiation, growth, and progression⁶³, where it regulates protein synthesis through two downstream arms: the 4E-BP1-eIF4E axis and the S6K-rpS6 axis⁶⁴. With *HMG2* knockdown, mTOR phosphorylation was unaltered, as was 4E-BP1, a negative regulator of translation initiation (Supplementary Fig. 4a–b). However, we consistently observed decreased S6K phosphorylation at T389, a critical activation site, and decreased phosphorylation of downstream targets rpS6 and eIF4B (Fig. 4a). To confirm that *HMG2*^{high} cell lines rely on high levels of pS6K, we knocked down *S6KB1* in human PDAC lines and observed significant growth defects and cell death in basal but not classical PDAC (Fig. 4b, Supplementary Fig. 4c). Additionally, ectopic expression of wildtype S6K (WT-S6K) or a constitutively active S6K (CA-S6K) could rescue S6K signaling after *HMG2* knockdown in human basal PDAC (Fig. 4c).

S6K has been shown to be a critical mediator of mRNA translation by controlling translation initiation and elongation⁶⁵. To determine if these same steps are regulated by *HMG2*, we performed polysome profiling and observed a decrease in polysomes upon loss of *HMG2*

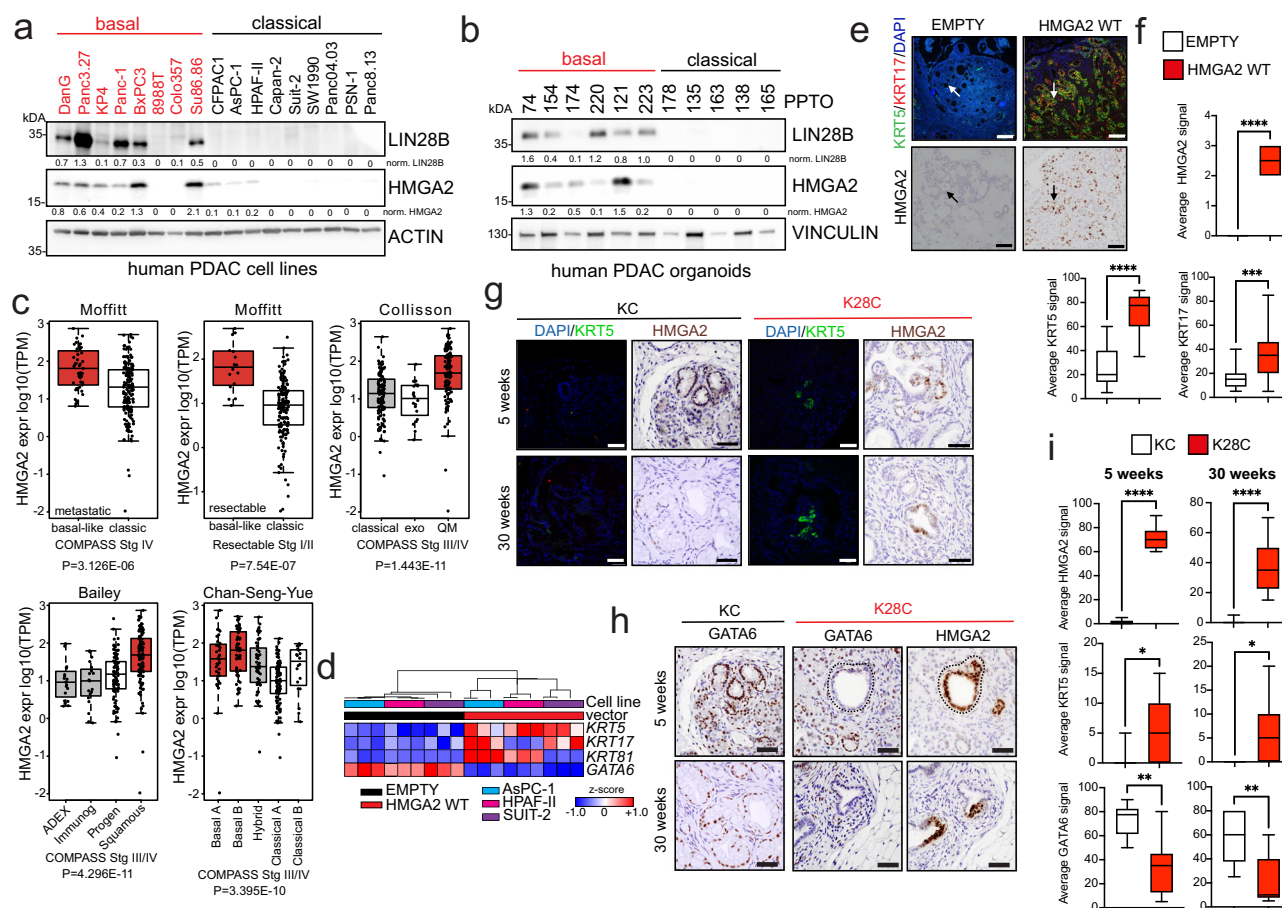


Fig. 3 | HMG2 strongly associates with the basal subtype. a WB of LIN28B, HMG2 and ACTIN from whole cell lysates of human PDAC cell lines. **b** WB of LIN28B, HMG2 and VINCULIN from whole cell lysates of human PDAC cell lines. **c** Gene expression of HMG2 in COMPASS trial data analyzed using indicated subtyping algorithms. **d** Hierarchical clustering and gene expression analysis using qRT-PCR in three classical PDAC cell lines engineered to overexpress an empty vector control or HMG2 WT upon doxycycline treatment. **e–f** Immunofluorescence for DAPI, KRT5, KRT17 (**e**) and immunohistochemistry for HMG2 in engineered Capan-2 xenografts. Cells overexpress WT HMG2 or an empty vector. Scale bars = 100 μ m. Orthotopic implants in NSG mice, treated with 200 μ g/mL doxycycline post-surgery. Arrows and dotted lines comparable glands. Quantification of the average signal of the indicated antibodies (**f**).

g–i Immunofluorescence for DAPI, KRT5 (**g**), immunohistochemistry for GATA6 and HMG2 (**g–h**) in K28C and KC timepoint mice. Scale bars = 50 μ m. Quantification of the average signal of the indicated antibodies (**i**). IF and IHC of KC represent the same region, therefore HMG2 IHC is not shown. Box plots (**f**, **i**) represent median, interquartile range and 5–95th percentile of $n = 5$ mice. Asterisks, P values after unpaired, two-tailed t test. **** $P < 0.0001$ HMG2 WT vs EMPTY, HMG2; **** $P < 0.0001$ HMG2 WT vs EMPTY, KRT5; *** $P = 0.0006$ HMG2 WT vs EMPTY, KRT17; **** $P < 0.0001$ K28C vs KC, 5 weeks HMG2; **** $P < 0.0001$ K28C vs KC 30 weeks, HMG2; * $P = 0.0250$ K28C vs KC, 5 weeks KRT5; * $P = 0.0357$ K28C vs KC, 30 weeks KRT5; ** $P = 0.0023$ K28C vs KC, 5 weeks GATA6; ** $P = 0.0026$ K28C vs KC, 30 weeks GATA6; Source data are provided as a Source Data file.

(Fig. 4d). These findings suggest that HMG2 regulates translation initiation through S6K activation. We next asked if these changes in S6K signaling and ribosome loading are critical for protein synthesis rates in basal PDAC. At baseline, basal PDAC has remarkably elevated levels of de novo protein synthesis compared to classical PDAC in patient-derived cell lines and organoids, as measured by puromycin incorporation (Fig. 4e–f). Knockdown of *HMG2* in four basal cell lines (Fig. 4g) reduced protein synthesis, while classical lines were unaffected.

We observed that WT HMG2 expression was sufficient to increase pS6K (Fig. 5a) and de novo protein synthesis in classical PDAC lines (Fig. 5b). To determine if this increase in protein synthesis and pS6K caused by HMG2 overexpression led to enhanced growth in vivo, we implanted classical cell lines with or without HMG2 expression subcutaneously and orthotopically and observed accelerated tumor growth with WT HMG2 compared to control (Fig. 5c). Moreover, HMG2 expression reduced survival (Fig. 5d) and led to the formation of earlier metastases (Fig. 5e). IHC staining of tumors demonstrated higher levels of pS6K with WT HMG2 compared to the

empty vector (Fig. 5f–g). Together, our work supports the critical role of HMG2 in defining the lethal basal PDAC phenotype, regulating S6K and mRNA translation, and controlling tumor growth in vivo.

HMG2 controls mRNA translation downstream of LIN28B

We next sought to determine if the increase in protein synthesis we observe with high levels of HMG2 was recapitulated in our K28C mouse model. Indeed, protein de novo synthesis was increased in K28C mouse cell lines as compared to KC (Supplementary Fig. 5a). Daley and colleagues previously reported LIN28B-mediated let-7 independent regulation of protein synthesis in neuroblastoma that involved direct binding of LIN28B to mRNA transcripts of protein synthesis genes, resulting in their enhanced translation and expression⁶⁶. We examined our human model systems to determine if our observed phenotypes were LIN28B-dependent. In human cell lines, when LIN28B was knocked down in basal PDAC, reduction in de novo protein synthesis could be rescued with overexpression of HMG2 that contains no 3'UTR and thus lacks all let-7 binding sites (Supplementary Fig. 5b). Similarly, overexpression of LIN28B in classical cell

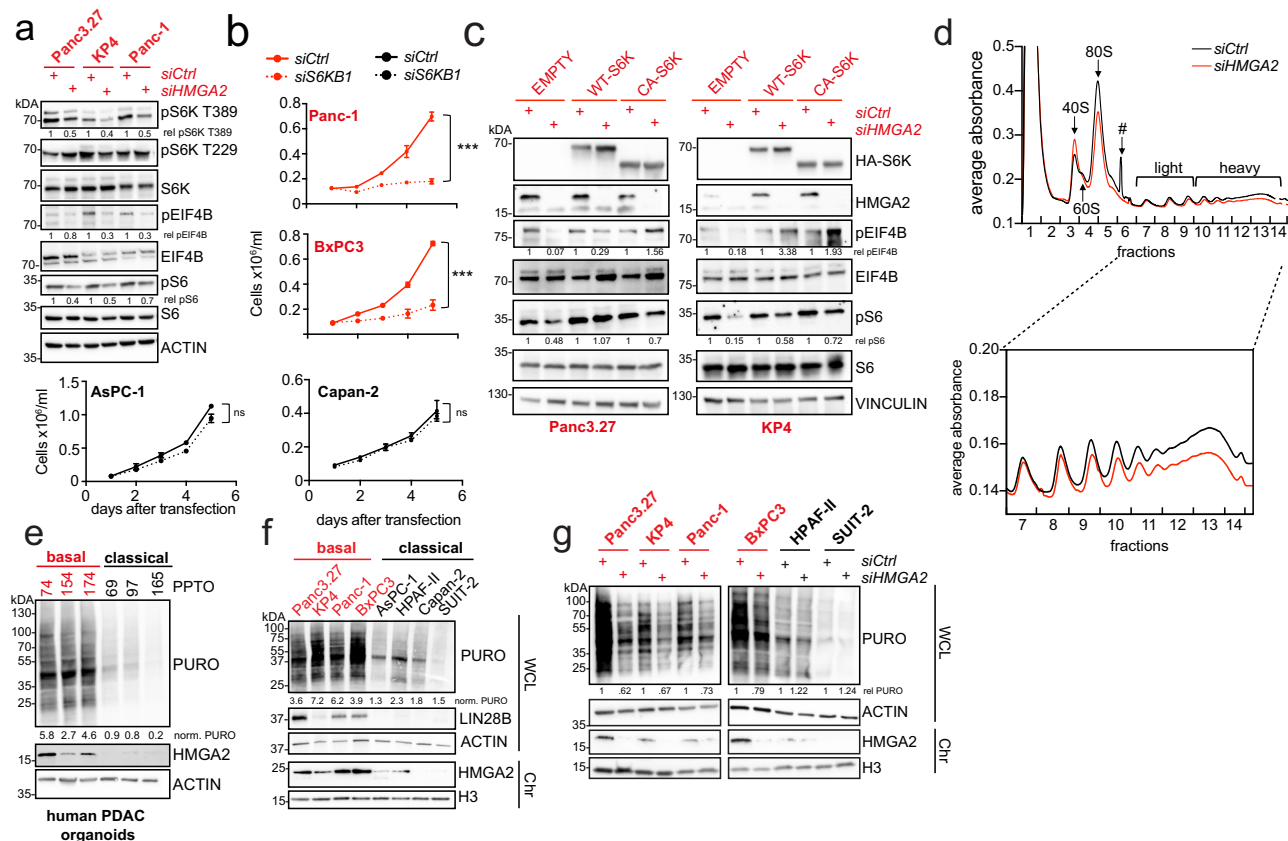


Fig. 4 | High expression of HMGA2 leads to dramatic changes in protein synthesis. **a** WB for pS6K T389 and pS6K T229, S6K, pEIF4B S422, EIF4B, pS6 S235/S236, S6, and ACTIN in basal PDAC cell lines transfected with an siRNA against a non-targeting control or *HMGA2*. **b** Growth curves of two basal and two classical PDAC cell lines transfected with siRNA against *S6KB1* or a non-targeting control. Data are displayed as means \pm s.e.m ($n = 3$ biologically independent experiments); asterisks, P values after unpaired, two-tailed t test. *** $P = 0.0002$ siS6KB1 vs siCtrl, Panc-1; *** $P = 0.0004$ siS6KB1 vs siCtrl, BxPC3; ns, non-significant. **c** WB for HA-S6K, HMGA2, pS6K T389, S6K, pEIF4B S422, EIF4B, pS6 S235/S236, S6, and VINCULIN in human basal PDAC cell lines engineered to overexpress an empty control, HA-tagged wildtype S6K (WT-S6K) or a constitutively active S6K (CA-S6K) upon doxycycline treatment. Cells were transfected with siRNA against *HMGA2* or a non-

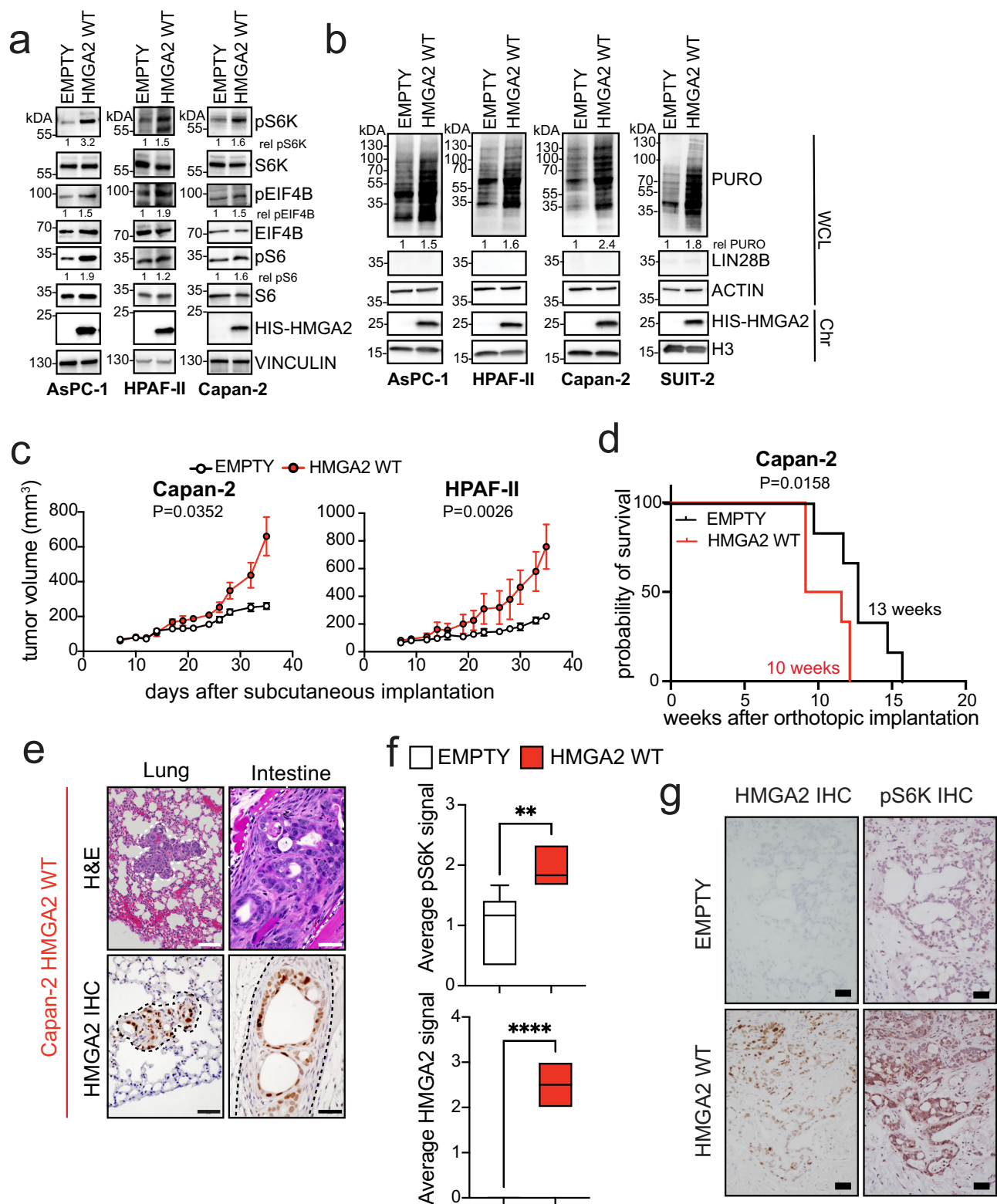
targeting control. **d** Full polysome profiling traces for KP4 cell line transfected with siRNA against *HMGA2* or a non-targeting control from triplicate experiments. The experiment has been repeated twice with similar results. Arrows: 40S, 60S, and 80S peaks; #: DNA contamination; light and heavy polysome fractions. **e** WB for puromycin incorporation, HMGA2, and ACTIN in three basal and three classical human PDAC organoids. **f** WB for puromycin incorporation, LIN28B, ACTIN, HMGA2, and H3 in basal and classical PDAC lines. WCL, whole cell lysates; Chr, chromatin. **g** WB for puromycin incorporation, ACTIN, HMGA2, and H3 in four basal and two classical PDAC lines transfected with siRNA targeting *HMGA2* or a non-targeting control. WCL, whole cell lysates; Chr, chromatin. Source data are provided as a Source Data file.

lines resulted in elevated endogenous HMGA2 levels, which subsequently enhanced de novo protein synthesis. Conversely, knockdown of *HMGA2* in cells with exogenous *LIN28B* expression prevented this increase in protein synthesis (Supplementary Fig. 5c). Lastly, knockdown of *Hmga2* in K28C mouse cell lines reduced de novo protein synthesis (Supplementary Fig. 5d). These findings suggest that HMGA2 modulates global mRNA translation downstream of LIN28B.

HMGA2 controls S6K phosphorylation through LCMT1 and specific methylation of PP2A

We have demonstrated that loss of HMGA2 in basal PDAC reduces phosphorylation of S6K at T389 by ~50%, which is consistent with the extent of reduction in protein synthesis we observe (Fig. 4a, g). However, we saw no evidence that either upstream or downstream components of the mTOR pathway were affected by loss of HMGA2, except for S6K phosphorylation (Supplementary Fig. 4a–b). This would suggest that HMGA2 may regulate S6K in an mTOR-independent manner. Since mTOR is the only known kinase capable of phosphorylating T389 of S6K, we hypothesized that a phosphatase may be recruited for HMGA2-mediated regulation of S6K⁶⁷. Of the known human phosphatases, PP2A has been shown to directly bind to S6K and dephosphorylate T389 without affecting phosphorylation of other mTOR

substrates, including AKT or 4E-BP1⁶⁸. The PP2A holoenzyme is composed of three subunits: *A* (scaffold), *B* (regulatory), and *C* (catalytic). While the human genome encodes only two PP2A-A subunits and two PP2A-C subunits, there are at least 12 different PP2A-B genes that allow for regulation and substrate specificity⁶⁹. To determine if PP2A is responsible for S6K dephosphorylation, we knocked down the catalytic subunits of PP2A. Interestingly, knockdown of the more abundant subunit, *PPP2CA*, restored pS6K in the context of HMGA2 loss (Fig. 6a–b). For orthogonal validation, we treated *HMGA2* knockdown cells with okadaic acid, an inhibitor of serine/threonine phosphatases including PP2A, and observed rescue of pS6K (Fig. 6c). PP2A catalytic activity is modulated by several post-translational modifications, with the carboxymethylation of the terminal leucine residue on the catalytic subunit driving biased heterotrimerization and enhancing PP2A's tumor suppressive activity⁷⁰. Loss of HMGA2 in basal lines led to increased mePP2A while overexpression of HMGA2 in classical lines decreased mePP2A (Fig. 6d–e). Carboxymethylation of this residue is catalyzed by the leucine carboxyl methyltransferase 1 (LCMT1). Interestingly, knockdown of *HMGA2* resulted in increased *LCMT1* expression (Fig. 6f–g) while HMGA2 overexpression in classical lines reduced its expression (Fig. 6h). When we performed chromatin immunoprecipitation (ChIP) at the *LCMT1* promoter, we found that HMGA2 bound



within 500 bp of the transcription start site. Furthermore, knockdown of *HMGA2* led to increases in active transcription marks H3K4me3 and RNA Pol II serine 5 phosphorylation at the same locus (Fig. 6i). To determine whether modulation of *LCMT1* itself could control mRNA translation, we overexpressed WT *LCMT1* in basal lines and found increased mP2AC, reduced pS6K, and decreased mRNA translation (Fig. 7a). Conversely, when we knocked down *LCMT1* in classical lines, we observed increased mRNA translation (Fig. 7b) and a gain of basal features as measured by *KRT5*, *KRT17*, and *KRT81* (Fig. 7c). Upon

subcutaneous injection, sh*LCMT1* cells exhibited enhanced tumor growth (Fig. 7d) and greater tissue invasion (Fig. 7e) compared to shCtrl xenografts. Additionally, sh*LCMT1* tumors displayed elevated expression of *KRT5* and *KRT81* (Fig. 7f–g), along with increased pS6K levels (Fig. 7h), mirroring the *HMGA2* WT phenotype. Thus, *HMGA2* modulates pS6K levels and protein synthesis through transcriptional downregulation of *LCMT1*, resulting in decreased PP2A methylation and activity and regulation of lineage plasticity (see Fig. 7i for proposed model).

Fig. 5 | Overexpression of HMGA2 in classical PDAC results in more aggressive disease and higher levels of pS6K in vivo. **a** WB for pS6K T389, total S6K, pEIF4B S422, total EIF4B, pS6 S235/S236, total S6, and His-tagged HMGA2 in three classical PDAC cell lines engineered to overexpress empty vector or HMGA2 WT upon doxycycline treatment. **b** WB of puromycin incorporation, LIN28B, ACTIN, His-tagged HMGA2, and H3 in four HMGA2^{low} PDAC cell lines engineered to overexpress empty or HMGA2 WT upon doxycycline treatment. WCL, whole cell lysate; Chr, chromatin. **c** Engineered Capan-2 and HPAF-II cells outgrow control cells when overexpressing WT HMGA2 (red). Subcutaneous flank implants in NSG mice, treated with 200 µg/mL doxycycline post-surgery. Data are displayed as means ± s.e.m. N(Capan-2 Empty) = 4 mice, N(Capan-2 WT HMGA2) = 4 mice, N(HPAF-II Empty) = 4 mice and N(HPAF-II WT HMGA2) = 4 mice; *P* values after paired, two-tailed *t* test. **d** Tumor-free survival curve for mice orthotopically implanted with the

indicated engineered Capan-2 cell lines. N(Capan-2 Empty) = 6 mice and N(Capan-2 WT HMGA2) = 6 mice; *P* values after log-rank test. NSG mice were treated with 200 µg/mL doxycycline post-surgery. **e** Metastases to the lung (left, scale bar = 50 µm) and small intestine (right, scale bar = 100 µm) were observed with HMGA2-overexpressing tumors. Specific immunohistochemistry for HMGA2. Scale bar = 50 µm. **f** Quantification of specific immunohistochemistry for HMGA2 and pS6K T389 in HMGA2 WT tumors compared to empty vector control of orthotopically implanted engineered Capan-2 cells from Fig. 5d. Box plots represent median, interquartile range and 5–95th percentile of *n* = 6 mice. Asterisks, *P* values after unpaired, two-tailed *t* test. ***P* = 0.005 HMGA2 WT vs EMPTY, pS6K; *****P* < 0.0001 HMGA2 WT vs EMPTY, HMGA2. **g** Representative HMGA2 and pS6K IHC images. Scale bar = 50 µm. Source data are provided as a Source Data file.

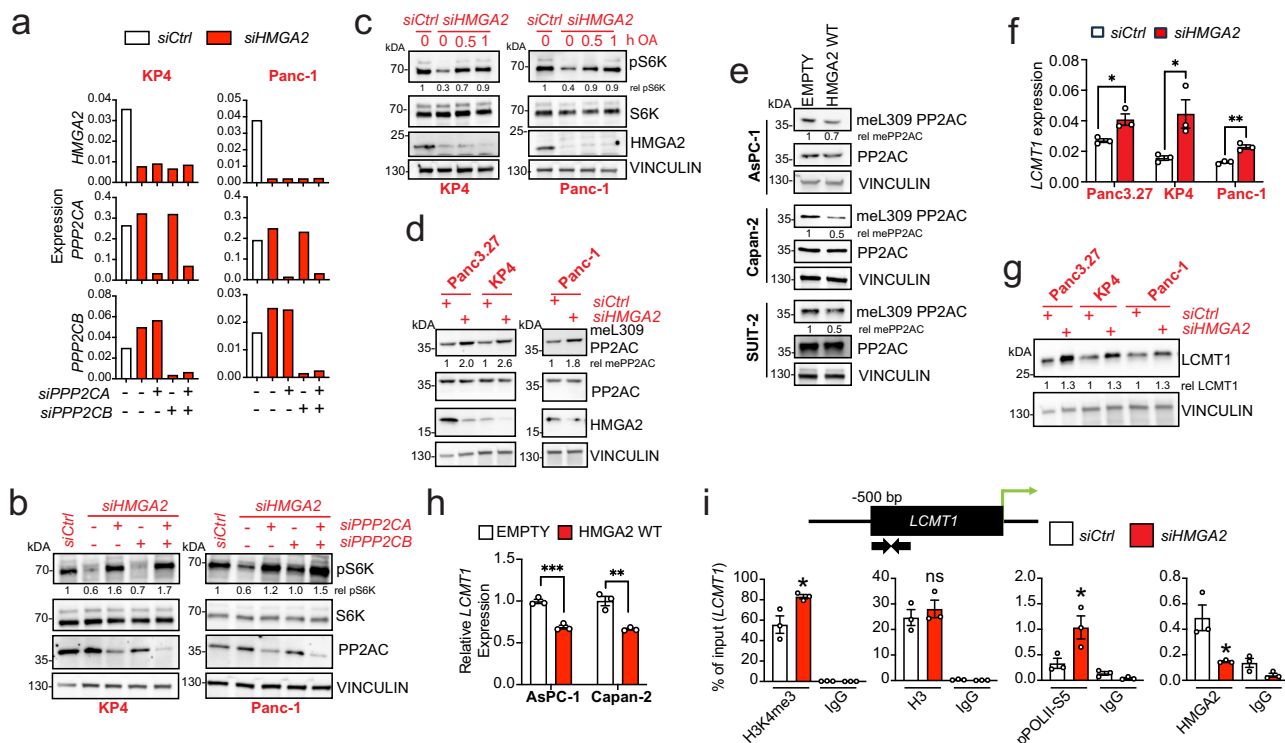


Fig. 6 | HMGA2 controls activation of PP2A and LCMT1. **a** QRT-PCR for *HMGA2*, *PPP2CA*, and *PPP2CB* in two HMGA2 high cell lines transfected with an siRNA against a non-targeting control, *HMGA2*, *PPP2CA*, and *PPP2CB* as indicated. Plots are displayed as means of technical triplicates. **b** WB for pS6K T389, total S6K, PP2AC, and VINCULIN in two HMGA2 high cell lines transfected with an siRNA against a non-targeting control, *HMGA2*, *PPP2CA*, and *PPP2CB* as indicated. **c** WB for pS6K T389, S6K, HMGA2, and VINCULIN in two basal PDAC cell lines transfected with an siRNA against a non-targeting control or *HMGA2*, then treated with 100 nM okadaic acid (OA) for the indicated times. **d** WB for meL309 PP2AC, total PP2AC, HMGA2, and VINCULIN in three basal PDAC cell lines transfected with an siRNA against a non-targeting control or *HMGA2*. **e** WB of meL309 PP2AC, PP2AC, and VINCULIN in three classical PDAC cell lines engineered to overexpress empty or HMGA2 WT upon doxycycline treatment. **f–g** QRT-PCR (**f**) and WB (**g**) for LCMT1 in three basal

PDAC cell lines transfected with siRNA against a non-targeting control or *HMGA2*. Bar plots are displayed as mean ± s.e.m. (*n* = 3 biologically independent experiments); asterisks, *P* values after unpaired, two-tailed *t* test. **P* = 0.0245 siHMGA2 vs siCtrl, Panc3.27; **P* = 0.0374 siHMGA2 vs siCtrl, KP4; ***P* = 0.0027 siHMGA2 vs siCtrl, Panc-1. **h** QRT-PCR for LCMT1 in two classical PDAC cell lines engineered to overexpress HMGA2 upon dox-treatment. **i** ChIP for H3K4me3, H3, serine 5 phosphorylated RNA Pol II, HMGA2, and IgG at the LCMT1 promoter in KP4 cells transfected with siRNA against a non-targeting control or *HMGA2*. Bar plots (**h–i**) are displayed as mean ± s.e.m. (*n* = 3 biologically independent experiments); asterisks, *P* values after unpaired, two-tailed *t* test. ****P* = 0.0008 HMGA2 WT vs EMPTY, AsPC-1; ***P* = 0.0041 HMGA2 WT vs EMPTY, Capan-2; **P* = 0.0356 siHMGA2 vs siCtrl H3K4me3; **P* = 0.0459 siHMGA2 vs siCtrl pPolII; **P* = 0.0268 siHMGA2 vs siCtrl HMGA2; ns, non-significant. Source data are provided as a Source Data file.

HMGA2 disrupts PPP2R5A-PP2A targeting of phosphorylated S6K in PDAC cells

To investigate whether HMGA2 influences the formation of the PP2A holoenzyme responsible for targeting phosphorylated S6K, we leveraged DT-061, a small-molecule PP2A activator known to promote active PP2A holoenzyme assembly⁷¹. Prolonged treatment of basal PDAC cells with DT-061 resulted in a marked decrease in de novo protein synthesis, accompanied by increased formation of mePP2A heterotrimers and reduced pS6K levels, phenocopying HMGA2's

effects on LCMT1 (Supplementary Fig. 6a). Notably, DT-061 functions as a molecular glue, stabilizing the interaction between the PPP2R5A (B56α) regulatory subunit and PP2A⁷². To determine HMGA2's influence on *PPP2R5A* expression, we performed *HMGA2* knockdown in basal PDAC cells, which significantly increased *PPP2R5A* levels (Supplementary Fig. 6b–c). When we performed ChIP at the *PPP2R5A* promoter, we found that HMGA2 was enriched at the transcription start site. Knockdown of *HMGA2* led to increases in active transcription marks H3K4me3 and RNAPII serine 5 phosphorylation at the promoter

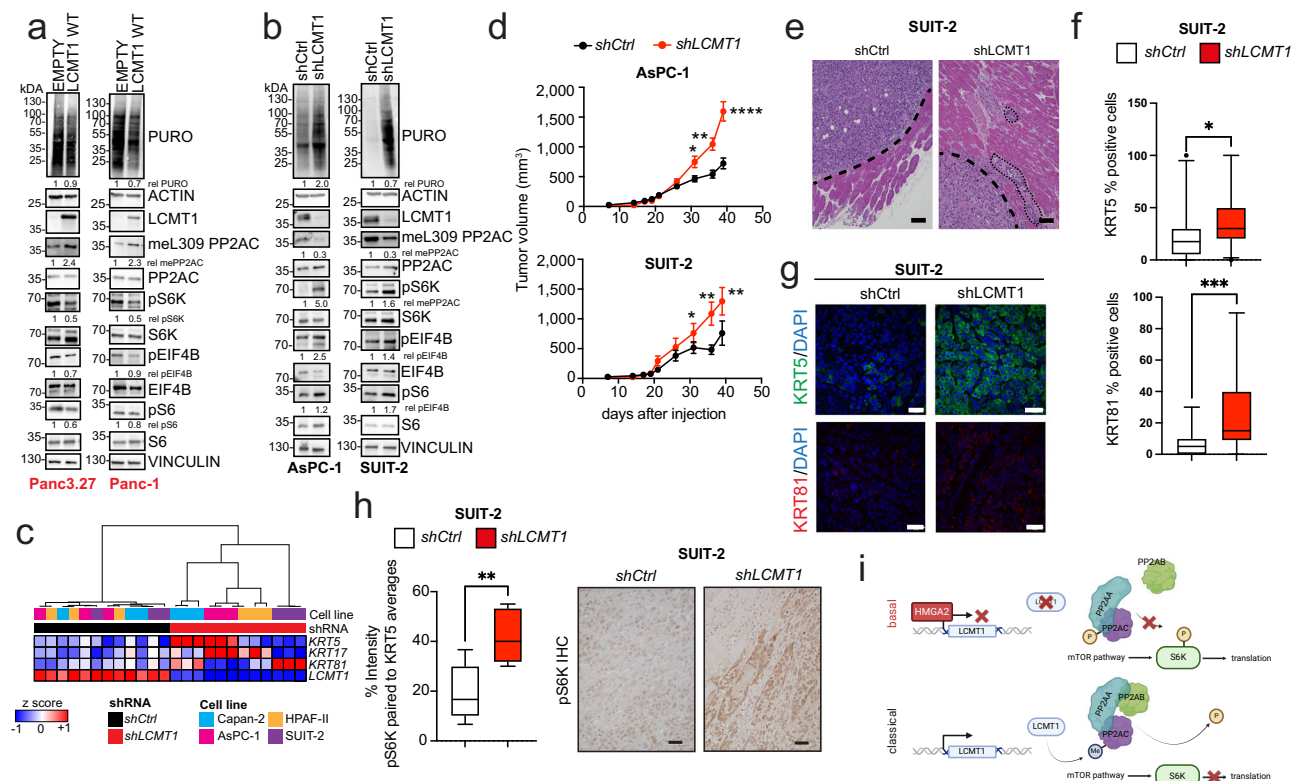


Fig. 7 | Loss of LCMT1 recapitulates phenotype of HMGA2^{high} PDAC. **a** WB of puromycin incorporation, ACTIN, LCMT1, meL309 PP2AC, total PP2AC, pS6K T389, S6K, pEIF4B, EIF4B, pS6, S6, and VINCULIN in two basal cell lines stably transduced with LCMT1 WT or a control vector. **b** WB of puromycin incorporation, ACTIN, LCMT1, meL309 PP2AC, total PP2AC, pS6K T389, S6K, pEIF4B S422, EIF4B, pS6 S235/S236, S6, and VINCULIN in two classical cell lines stably transduced with shRNA targeting *LCMT1* or a non-targeting control. **c** Hierarchical clustering and gene expression analysis using qRT-PCR for *KRT5*, *KRT17*, *KRT81*, and *LCMT1* in four classical PDAC cell lines stably transduced with shRNA targeting *LCMT1* or a non-targeting control. **d** Engineered AsPC-1 and SUI-2 cells stably expressing shRNA scrambled (black) or shRNA against *LCMT1* (red) were injected subcutaneously into flanks of NSG mice. Data are represented as mean ± SEM. N(AsPC-1) = 10 and n(SUI-2) = 8; asterisks, *P* values after unpaired, two-tailed *t* test. **P* = 0.0187 shLCMT1 vs shCtrl, day 31 AsPC-1; ***P* = 0.0017 shLCMT1 vs shCtrl, day 36 AsPC-1; *****P* < 0.0001 shLCMT1 vs shCtrl, day 39 AsPC-1; **P* = 0.0364 shLCMT1 vs shCtrl, day 31 SUI-2; ***P* = 0.0038 shLCMT1 vs shCtrl, day 36 SUI-2; ***P* = 0.0014 shLCMT1 vs shCtrl, day SUI-2. **e** Representative H&E images of the invasive phenotype of shLCMT1

cell lines. Dashed line represents tumor border, dotted line indicates tumor cells invading into muscle. Scale bar = 100 μm. **f–g**, Quantification of area signal of the indicated antibodies (**f**) and immunofluorescence for DAPI, KRT5, and KRT81 (**g**) in engineered SUI2 xenografts. Cells overexpress shControl or shLCMT1. Box plots represent median, interquartile range and 5th to 95th percentile of *n*(KRT5 shCtrl) = 24, *n*(KRT5 shLCMT1) = 27, *n*(KRT81 shCtrl) = 27 and *n*(KRT81 shLCMT1) = 26 different areas in seven mice; asterisks, *P* values after unpaired, two-tailed *t* test. **P* = 0.0270 shCtrl vs shLCMT1 KRT5; ****P* = 0.0007 shCtrl vs shLCMT1 KRT81. **h** left: Quantification of pS6K T389 in KRT5-positive subcutaneous tumors from Fig. 7d–g. Box plots represent median, interquartile range and 5–95th percentile of *n* = 7 mice; asterisks, *P* values after unpaired, two-tailed *t* test. ***P* = 0.0020 shLCMT1 vs shCtrl SUI-2. Right: Representative images of pS6K T389 IHC of the indicated xenografts. Scale bar = 50 μm. **i**, Model of proposed mechanism by which HMGA2 controls translation levels via suppression of LCMT1 and deactivation of PP2A. Created in BioRender. Yamamoto, N. (2025) <https://BioRender.com/s26w133>. Source data are provided as a Source Data file.

(Supplementary Fig. 6d). Importantly, HMGA2 loss did not affect the expression of the PP2A scaffold (A subunit) or the catalytic PP2AC subunit (Supplementary Fig. 6e). To explore whether HMGA2 loss altered PPP2R5A/PP2AC interactions, we performed sucrose ultracentrifugation of native protein lysates to analyze changes in PP2A complex formation. In basal cells at baseline, active PP2A, comprising mePP2A and PPP2R5A, was not associated with phosphorylated S6K (Supplementary Fig. 6f). However, knockdown of *HMGA2* led to co-sedimentation of phosphorylated S6K, mePP2A, and PPP2R5A. Together, our findings indicate that through suppression of LCMT1 and PPP2R5A, HMGA2 prevents formation of the active PP2A holoenzyme and leads to increased phosphorylated S6K.

Targeting protein synthesis in basal PDAC

Our data suggest that, compared to classical PDAC, basal PDAC may be intrinsically dependent on increased protein synthesis via the HMGA2-S6K axis (Figs. 4–5). It has been shown that the small molecule homoharringtonine (HHT) inhibits translationally-driven tumors by

halting translation initiation after the ATG start codon⁷³. Given HMGA2's profound impact on translation initiation, we wondered if it could dictate HHT sensitivity. HHT treatment reduced mRNA translation in both HMGA2^{high} basal and HMGA2^{low} classical human and murine PDAC lines, but only HMGA2^{high} lines underwent cell death, as measured with cleaved PARP or crystal violet assay (Fig. 8a–d). Additionally, overexpression of WT HMGA2 in classical lines increased sensitivity to HHT (Fig. 8e). We next used a PDX model subtyped as basal and confirmed high expression of HMGA2 by IHC (Fig. 8f). The model was treated with HHT for 21 days, and growth was significantly inhibited compared to vehicle (Fig. 8g). In comparison, classical PDXs were not sensitive (Fig. 8h). HHT also did not cause substantial toxicity, as assessed by maintenance of animal weight throughout treatment (Fig. 8i–j). Additionally, treatment with HHT resulted in prolonged survival of basal PDXs (Fig. 8k). Together, these studies demonstrate that high levels of mRNA translation and active S6K are required for growth in HMGA2^{high} but not HMGA2^{low} PDAC, defining a potential therapeutic strategy.

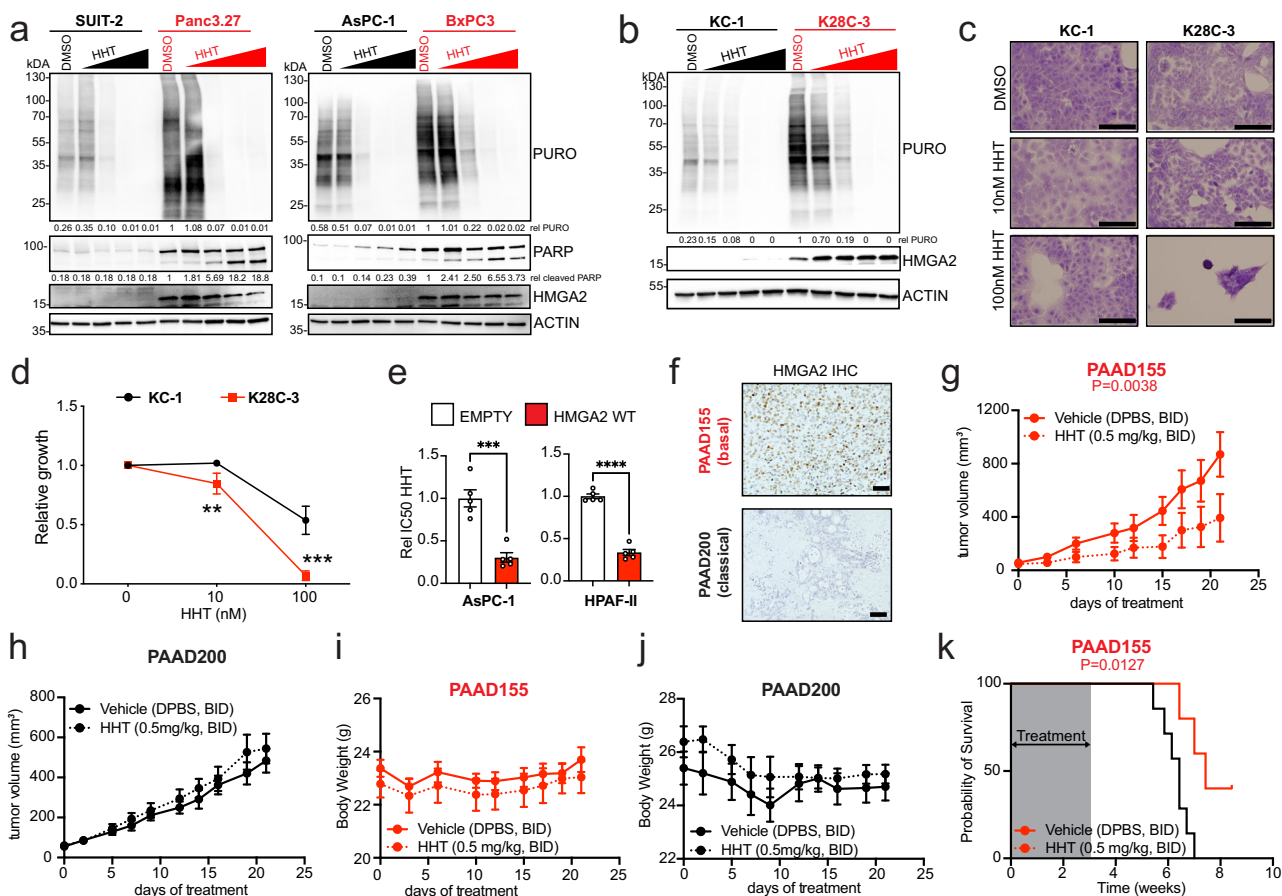


Fig. 8 | Targeting protein synthesis in basal PDAC. **a** WB of puromycin incorporation, PARP, HMGA2, and ACTIN in two basal and two classical cell lines treated with homoharringtonine (HHT). **b** WB of puromycin incorporation, HMGA2, and ACTIN in KC and K28C cell lines treated with HHT for 24 h. **c–d**, Representative brightfield color images of crystal violet-staining (**c**) and relative growth (**d**) of KC and K28C murine PDA cells treated with increasing doses of HHT for 24 h. Scale bar = 100 μ m. Data are displayed as means \pm s.e.m. ($n = 4$ biological replicates); asterisks, P values after unpaired, two-tailed t test. **e** Relative IC₅₀s of two classical PDAC lines engineered to overexpress HMGA2 upon dox-treatment. Cells were treated with increasing doses of HHT. Data are displayed as means \pm s.e.m. ($n = 5$ biological replicates); asterisks, P values after unpaired, two-tailed t test. **f** Immunohistochemistry for HMGA2 in one basal (PAAD155) and one classical (PAAD200) PDX model. Scale bar = 100 μ m. **g–h**, Tumor volume of PAAD155 (**g**) and PAAD200 (**h**) xenografts after treatment with twice-daily HHT (0.5 mg/kg, dashed) compared with vehicle control (DPBS, solid) for 21 days. **i–j**, Whole-body weights of mice implanted with PAAD155 (**i**) and PAAD200 (**j**) xenografts after treatment with twice-daily HHT (0.5 mg/kg, dashed) compared with vehicle control (DPBS, solid) for 21 days. **k** The PAAD155 cohort in (**g**) was monitored for survival up to 8 weeks after treatment. Kaplan-Meier analysis and log-rank P values are shown between groups. Source data are provided as a Source Data file.

Discussion

Our study demonstrates that the oncofetal proteins LIN28B and HMGA2 are highly expressed in basal subtype PDAC and that basal PDAC model systems are uniquely reliant on LIN28B/HMGA2 for cell growth. By using the p48-Cre; KrasG12D mouse model, we show that LIN28B expression accelerates autochthonous KrasG12D-driven pancreatic cancer. Downstream of LIN28B, we show that HMGA2 drives increased expression of basal PDAC markers and alters protein synthesis by regulating phosphorylation of S6K. Mechanistically, HMGA2 reduces the expression of the methyltransferase LCMT1 and PPP2R5A, leading to decreased PP2A methylation and activity. The resulting elevated levels of S6K phosphorylation and overall protein synthesis renders basal PDAC hypersensitive to protein synthesis inhibition by HHT. Likewise, ectopic expression of HMGA2 in classical cell lines sensitized these cells to protein synthesis inhibition. This study describes a mechanism by which HMGA2 expression contributes to aggressive PDAC and proposes targeted therapies for treatment of these subtypes.

Reactivated expression of LIN28B and HMGA2 has previously been described in pancreatic cancer and distant metastasis. However, how the LIN28B/HMGA2 axis promotes pancreatic cancer initiation and progression has remained a mystery. Here, we demonstrate that sustained expression of LIN28B in a PDAC GEMM accelerates tumorigenesis, metastasis and decreases survival compared to littermates without LIN28B expression. These findings are consistent with those of Franses and colleagues, who identified that LIN28B expression in circulating tumor cells was prognostic for poor survival²². We found that continuous expression of LIN28B is required for an accelerated disease phenotype. This is consistent with LIN28B's role in upregulating HMGA2, which we found to be both necessary and sufficient for PDAC survival. Furthermore, we observed that ectopic expression of HMGA2 in the absence of LIN28B was sufficient to increase tumor growth and metastatic potential in vivo. These findings suggest that LIN28B's oncogenic function in pancreatic cancer is primarily through its role in upregulating HMGA2.

HMGA2 is overexpressed in pancreatic cancer tissues compared to adjacent normal ducts, underscoring its potential diagnostic and

prognostic value⁷⁴. Numerous studies have established correlations between elevated HMGA2 levels and more undifferentiated tumor histology, advanced stage, and lymph node metastasis, implicating HMGA2 in driving disease progression and aggressiveness in PDAC and other malignancies^{75,76}. Moreover, HMGA2's association with chemotherapy resistance in cancer cell lines further accentuates its clinical significance, indicating its potential as a therapeutic target to improve treatment outcomes⁷⁷.

In the study by Chiao and colleagues⁵⁰, the loss of HMGA2 in the KPC mouse model did not significantly affect survival or metastatic burden. This outcome is likely due to the enforced loss or mutation of p53 in the KPC model, which bypasses the dependency on HMGA2 for tumor progression. In contrast, our K28C mouse model introduces HMGA2 gain-of-function (GOF) paired with stochastic loss or decreased function of p53, resulting in tumors that are highly dependent on HMGA2. The loss of p53 during tumor progression in the K28C model creates a unique genetic context in which HMGA2 GOF becomes indispensable. These results highlight the critical influence of genetic context, particularly the difference between p53 loss in utero versus during tumor progression on tumor dependencies.

Recent studies have emphasized the importance of the cell of origin in determining PDAC subtypes and progression⁷⁸. For example, KRAS-driven tumors originating from acinar cells are predominantly enriched in the classical subtype, which is characterized by high expression of endodermal lineage markers, such as GATA transcription factors. While p53 inactivation or mutation accelerates tumorigenesis in these tumors, tumor initiation can still occur in the presence of wild-type p53, although at a slower pace. By contrast, tumors arising from ductal cells are frequently associated with the basal-like subtype, which is enriched for squamous lineage markers and exhibits a more aggressive phenotype. These ductal-derived tumors require p53 inactivation or mutation (e.g., Trp53R172H or Trp53R270H) to drive aggressive growth and metastasis. Interestingly, studies have also shown that the loss of tumor suppressors in mouse models can induce PDAC even in the context of wild-type p53, further supporting the notion that the cell of origin and genetic alterations work in concert to dictate tumor behavior.

Our findings align with these insights by demonstrating that LIN28B/HMGA2 GOF preferentially drives basal-like features in the context of p53 loss during tumor progression. Furthermore, our investigation revealed a strong association between HMGA2 expression patterns and the basal pancreatic cancer subtype. Notably, ectopic expression of HMGA2 in the classical PDAC subtype resulted in increased expression of basal keratins such as KRT5 and KRT17, alongside suppression of the classical marker GATA6. These findings highlight HMGA2's pivotal role in defining subtype specificity and shaping the molecular landscape of PDAC progression. Beyond its role as a prognostic marker, HMGA2 represents a key determinant of subtype specificity and offers potential avenues for targeted therapeutic interventions in basal-like PDAC.

Our work also identifies regulation of the phosphatase PP2A as a molecular switch in PDAC. PP2A negatively regulates several growth-related pathways including ERK, AKT, and WNT signaling⁷⁹ and suppresses c-MYC oncogenic activation⁸⁰. Inhibition of PP2A in cancer can occur through increased levels of endogenous inhibitors besides mutation in specific subunits⁸¹. CIP2A and SET are frequently over-expressed in pancreatic cancer and inhibit PP2A activity⁸². Its reduced activity increases cell growth and is strongly associated with epithelial-mesenchymal transition^{83,84} and MEK inhibitor resistance⁸⁵. Our study has established the relevance of PP2A in fine-tuning protein synthesis in pancreatic cancer. Interestingly, basal PDAC evolves to reduce PP2A activity by controlling the expression of the PP2A activator LCMT1.

By using complementary in vitro and in vivo models, we have identified a vulnerability of basal PDAC: protein synthesis. We found

that basal PDAC has much higher levels of de novo protein synthesis and is sensitive to loss of S6K or pharmacological inhibition. Homoharringtonine (HHT), also known as omacetaxine mepesuccinate, is a natural alkaloid derived from the *Cephalotaxus* genus of evergreen trees. Originally discovered in the 1970s, this compound has garnered significant attention due to its potent anti-cancer properties. One of the notable characteristics of HHT is its ability to inhibit protein synthesis by targeting the ribosome, leading to apoptosis in cancer cells. This mechanism makes it particularly effective against certain types of leukemia and solid tumors, including bladder, prostate, and lung cancer. HHT has been extensively studied and is approved by the Food and Drug Administration for the treatment of chronic myeloid leukemia⁸⁶. Treatment of lung cancer mouse models with HHT showed anti-cancer activity⁸⁷. Here, we demonstrate the relative efficacy of HHT in treating basal PDAC, demonstrating its potential use in subtype-specific therapies. Our study provides a vulnerability of basal PDAC that is directly actionable in the clinic to treat PDAC patients.

While HHT directly targets the identified pathway at the level of protein synthesis, alternative therapeutic strategies for basal PDAC could involve targeting S6K or modulating PP2A activity to disrupt the same pathway effectively. S6K inhibitors, such as LY2584702, have demonstrated efficacy in preclinical studies by suppressing S6K-mediated signaling pathways⁸⁸. However, a limitation of LY2584702 is that it does not address feedback activation of AKT through the mTORC1 pathway, a compensatory mechanism that can undermine its therapeutic effects. In contrast, M2698, a dual inhibitor of S6K and AKT1/3, offers a more comprehensive approach by concurrently targeting this feedback loop. Preclinical data indicate that M2698 reduces cell proliferation and tumor progression in mTOR-driven cancers, and its ability to penetrate the blood-brain barrier broadens its therapeutic potential⁸⁹. This dual action makes M2698 a more promising candidate, particularly in tumors like basal PDAC where mTOR signaling drives protein synthesis. Modulating PP2A activity presents another complementary therapeutic avenue. PP2A is a tumor suppressor, and its activity is often diminished in PDAC. Pharmacological activators of PP2A, such as DT-061, stabilize specific PP2A holoenzymes and restore its activity, leading to decreased pS6K levels⁷¹. This provides another mechanism to suppress protein synthesis and tumor growth in basal PDAC. By targeting S6K downstream of mTOR, DT-061 bypasses the need to directly inhibit mTOR itself, offering a distinct and potentially synergistic therapeutic pathway. In summary, targeting S6K activity with inhibitors like M2698, which addresses AKT feedback activation, or enhancing PP2A activity with activators like DT-061 to reduce pS6K levels, represents promising approaches for treating basal PDAC. These strategies not only converge on the regulation of protein synthesis but also provide complementary methods to disrupt key oncogenic pathways driving tumor progression.

While the dramatically high levels of protein synthesis we observe in basal PDAC provide an excellent target for therapeutic intervention, it remains unclear how the cell adapts to sustain this metabolic strain. Furthermore, it remains to be determined if specific pathways and proteins are over-expressed when HMGA2 levels are high, and how alteration of these pathways may provide other therapeutic targets for basal PDAC. Finally, HMGA2's regulation of LCMT1 and, therefore, mPP2A is not limited to its role in increasing pS6K and protein synthesis. LCMT1 also methylates the PP4 and PP6 protein phosphatases, thereby implicating HMGA2 in altering the general cellular phosphoproteome. The PP2A family is also implicated in a variety of cellular functions, including apoptosis, metabolism, cell mobility, and the cell cycle. The composition and relative abundance of different PP2A holoenzymes with and without HMGA2 present will provide

important opportunities for understanding the basic activity and specificity of this phosphatase.

Methods

Mice

Mice were housed in pathogen-free animal facilities under controlled conditions, including a 12 h light/dark cycle, an ambient temperature of 75 °F (24 °C), and a humidity level of 30–70%. All experiments were conducted under protocol PROTO201900024 in accordance with the Fred Hutchinson Cancer Center IACUC guidelines. *P48-Cre*⁹⁰ and *KrasLSL-G12D*⁹¹ mice were a kind gift from Sunil Hingorani. *P53flox* strain⁹² was a kind gift from Nabeel Bardeesy. *B6.Cg-Coll1a1tm2(tetO-LIN28B)Gqda/J*⁹³ and *B6.Cg-Gt(ROSA)26Sortm1(rtTA,EGFP)Nagy/J*⁹³ were purchased from Jackson (RRID:IMSR_JAX:005670 and RRI-D:IMSR_JAX:005670, respectively). Male *KrasLSL-G12D* +/-; *rtTA* +/- mice were crossed with female *P48-Cre* +/-; *tetO-LIN28B* mice to generate K28C, KC, LC, and C mice. Male *P53flox/flox* were crossed with female *P48-Cre* +/-; *KrasLSL-G12D* +/- mice to obtain KP^{+/+}-C mice. KP^{+/+}-C, K28C, KC, 28C, and C mice were maintained on a C57BL/6 background. NSG (NOD scid gamma) mice and homozygous NU/J mice were purchased from Translational Research Model Services Core (TRMS) at Fred Hutch Cancer Center and Jackson Laboratories (#002019), respectively. Data presented include both male and female mice. All mice in the survival analysis were euthanized upon reaching predefined disease burden criteria. Euthanasia was performed if animals exhibited one or more of the following conditions: tumor ulceration or necrosis, tumor bleeding or purulent discharge indicating infection, impaired mobility, inability to reach food or water, inability to remain upright, or interference with vital physiological functions (respiration, mastication, swallowing, urination, or defecation). Additional criteria included hunched posture for more than 48 h, labored breathing and/or cyanosis, severe dehydration, prolonged reduction in food intake, marked physical inactivity, weight loss exceeding 20% of normal body weight (monitored as part of tumor protocols), body condition score <2, persistent diarrhea or constipation for more than 48 hours, and severe anemia. Experimental K28C, KC, 28C, and C mice were fed with 200 µg/ml doxycycline in their drinking water upon weaning unless stated elsewhere.

Cell lines and organoids

Pancreatic cancer cell lines HPAF-II (CRL-1997), SW1990 (CRL-2172), PSN1 (CRL-3211), Panc03.27 (CRL-2549), Panc-1 (CRL-1469), BxPC3 (CRL-1687), Panc8.13 (CRL-2551), ASPC-1 (CRL-1682), and Capan-2 (HTB-80), CFPAC1 (CRL-1918), Panc04.03 (CRL-2555), and Su86.86 (CRL-1837) were obtained from American Type Culture Collection (ATCC; Rockville, MD). The DanG (ACC 249) and PaTu-8988t (ACC 162) pancreatic cancer cells were obtained from DSMZ, KP4 (JCRB0182) and SUIT-2 (JCRB1094) were obtained from JCRB cell bank, and COLO357 (Female 77 years) was a gift from Paul Chiao (MD Anderson). KP4, SW1990, PSN1, Panc03.27, BxPC3, Panc8.13, ASPC-1, Su86.86, DanG, SUIT-2, and COLO357 were grown in RPMI 1640 supplemented with 10% fetal bovine serum. Panc-1, CFPAC1, HPAF-II, and Capan-2 were grown in DMEM with 10% fetal bovine serum. Panc04.03 was grown in RPMI 1640 supplemented with 15% fetal bovine serum and 20 units/mL recombinant human insulin. Cells were passaged by trypsinization. All studies were done on cells cultivated for less than twenty passages. Human PDAC organoids were a kind gift from Faiyaz Notta. Mouse pancreatic organoids were derived and cultured according to the methods detailed in Tuveson Laboratory Murine and Human Organoid Protocols (https://tuvesonlab.labsites.cshl.edu/wp-content/uploads/sites/49/2018/06/20170523_OrganoidProtocols.pdf). Briefly, mouse tumor tissue was minced and digested in digestion media [DMEM + glucose, L-glutamine, sodium pyruvate (GIBCO) with 10% fetal bovine serum and 1% penicillin (100 U/ml)/streptomycin (100 Ug/ml) (Invitrogen GIBCO)] containing dispase (0.125 mg/ml, GIBCO) and

collagenase II (0.125 mg/ml, GIBCO) for 2 hours at 37 °C and 15 rpm. A fraction was seeded onto rat tail collagen coated plates to generate cell lines from the same tumors. The other tissue was further dissociated with TrypLE (GIBCO) for 15 min at 37 °C and 15 rpm. Cells were embedded in Matrigel and cultured in Mouse Feeding Medium (AdDMEM/F12 medium supplemented with HEPES [1×, Invitrogen], Glutamax [1×, Invitrogen], penicillin/streptomycin [1×, Invitrogen], B27 [1×, Invitrogen], Primocin [1 mg/ml, InvivoGen], N-acetyl-L-cysteine [200 µg/ml, Sigma], RSP01-conditioned medium [10% v/v], Mouse Noggin [0.1 µg/ml, Peprotech], Mouse EGF [50 ng/ml, Peprotech], Human Gastrin [0.21 µg/ml, Tocris], Human FGF10 [0.1 µg/ml, Preprotech], Y-27632 [0.21 µg/ml, Sigma], Nicotinamide [0.045 mg/ml, Sigma], and A83-01 [0.21 µg/ml, Tocris]). Organoids in this manuscript are labeled as 3D culture. To passage, murine organoids were disrupted in ice-cold splitting media (AdDMEM/F12 medium supplemented with HEPES [1×, Invitrogen], Glutamax [1×, Invitrogen], penicillin/streptomycin [1×, Invitrogen]), and human organoids were dissociated into single cells using TrypLE (GIBCO). Organoids were reseeded into Matrigel (Corning). Human organoids were cultured in Human Feeding Medium (AdDMEM/F12 medium supplemented with HEPES [1×, Invitrogen], Glutamax [1×, Invitrogen], penicillin/streptomycin [1×, Invitrogen], B27 [1×, Invitrogen], Primocin [1 mg/ml, InvivoGen], N-acetyl-L-cysteine [200 µg/ml, Sigma], Wnt3a-conditioned medium [20% v/v], RSP01-conditioned medium [30% v/v], Mouse Noggin [0.1 µg/ml, Peprotech], Human EGF [50 ng/ml, Peprotech], Human Gastrin [0.21 µg/ml, Tocris], Human FGF10 [0.1 µg/ml, Preprotech], Nicotinamide [0.045 mg/ml, Sigma], and A83-01 [0.21 µg/ml, Tocris]). Mouse cell lines/organoids used in this study are listed in Table S1. Quantitative PCR for *LIN28B*, *Lin28b*, *Hmga2*, and *Trp53* was performed to identify primary cell lines. No further authentication methods were used. Human pancreatic organoids derived from patients are listed in Table S2 and were authenticated via STR-profiling as indicated.

Whole cell lysates, chromatin isolation, and western blot

Chromatin fractions were prepared by resuspending the cell pellet in lysis buffer containing 10 mM HEPES pH 7.4, 10 mM KCl, 0.05% NP-40 supplemented with a protease inhibitor cocktail (Complete EDTA-free, Roche Applied Science), 5 µM TSA, 5 mM sodium butyrate, 1 mM DTT, and phosphatase inhibitors (Phosphatase Inhibitor Cocktail Sets I, II, and III Calbiochem) and incubated on ice for 20 min. The lysate was then centrifuged at 21,130 × g for 10 min at 4 °C. The supernatant was removed (cytosolic fraction) and the pellet (nuclei) was acid-extracted using 0.2 N HCl and incubated on ice for 20 min. The lysate was then centrifuged at 21,130 × g for 10 min at 4 °C. The supernatant (contains acid soluble proteins) was neutralized using 1 M Tris-HCl pH 8. For whole cell lysate (WCL), the cell pellet was resuspended in RIPA buffer (25 mM Tris-HCl pH 7.6, 150 mM NaCl, 1%NP-40, 0.5% sodium deoxycholate, 0.1% SDS) or NP40 lysis buffer (2.5 mM Tris-HCl pH7.5, 150 mM NaCl, 1%NP40, 10% Glycerol, 2 mM EDTA) supplemented with a protease inhibitor cocktail (Complete EDTA-free, Roche Applied Science), 5 µM TSA, 5 mM sodium butyrate, 1 mM DTT and phosphatase inhibitors (Phosphatase Inhibitor Cocktail Sets I, II and III, Calbiochem) and incubated on ice for 20 min. Cell lysates were sonicated for 30 s on/off for 10 min with 20% amplitude or 10 s on 20 s off for 1.5 min with 20% amplitude in RIPA or NP40 lysis buffer, respectively. The lysate was then centrifuged at 21,130 × g for 10 min at 4 °C and the supernatant was harvested. Protein concentration was quantified by BCA assay. Ten µg total protein (chromatin), or 20 µg (WCL) was electrophoresed on a 4–20% gradient polyacrylamide gel with SDS (Biorad) and electroblotted onto polyvinylidene difluoride membranes (PVDF) (Millipore). Membranes were blocked in TBS with 5% non-fat milk or 5% BSA (for phosphor-specific antibodies) and 0.1% Tween and probed with antibodies. Bound proteins were detected with horseradish-peroxidase-conjugated secondary antibodies

(1:5,000 Peroxidase Goat Anti-Rabbit IgG Antibody and 1:5,000 Peroxidase Horse Anti-Mouse IgG Antibody, Vector Biolaboratories PI-1000 and PI-2000, respectively) and Clarity Western ECL Max (Biorad) or Clarity Western ECL (Biorad). The following primary antibody dilutions were used: anti-HMGA2 (1:1000, Cell Signaling #5269), H3 (1:5000, Abcam #ab1791), anti-FLAG (1:1000, Sigma Aldrich #F1804), anti-IMP1 (1:1000, Cell Signaling #8482), anti-IGF2BP3 (1:1000, Proteintech #14642-1-AP), anti-b-actin (1:1000, Sigma Aldrich #A5316), anti-LIN28B (1:1000, Cell Signaling #4196), anti-pS6K T389 (1:1000, Cell Signaling #9234), anti-pS6K T229 (1:1000, R&D Biosystems #MAB8964-SP), anti-pS6 S235/236 (1:1000, Cell Signaling #4858), anti-S6K (1:1000, Cell Signaling #2708), anti-S6 (1:1000, Cell Signaling #2217), anti-pelf4B (1:1000, Cell Signaling #3591), anti-eIF4B (1:1000, CST #13088), anti-Puromycin (1:1000, Millipore #3591), anti-Vinculin (1:10,000, Millipore #V9131), anti-mEL309 PP2AC (1:500, Millipore MABE1809-25UL), anti-PP2AC (1:1000, Cell Signaling #2038), anti-LCMT1 6D9-G3 (1:200, Gift from Ogris Lab and Narla Lab), anti-PP2A A subunit (1:1000, Cell Signaling #2041 T), anti-B56alpha (1:500, Santa Cruz #sc-271151), anti-PARP (1:1000, Cell Signaling #9542), anti-pERK1/2 (1:1000, Cell Signaling #9101), anti-ERK1/2 (1:1000, Cell Signaling #4695), anti-pAKT (1:1000, Cell Signaling #13038), anti-AKT (1:1000, Cell Signaling #9272), anti-pmTOR S2481 (1:1000, Cell Signaling #2974), anti-pmTOR S2448 (1:1000, Cell Signaling #5536), anti-mTOR (1:1000, Cell Signaling #2972), anti-Beta-catenin (1:500, BD Biosciences #610154), anti-pP90 S380 (1:1000, Cell Signaling #11989), anti-pP90 T573 (1:1000, Cell Signaling #8743), anti-P90 (1:1000, Cell Signaling #9355), anti-p4E-BP1 (1:1000, Cell Signaling #2855), anti-4E-BP1 (1:1000, Cell Signaling #9644), anti-pEIF2K (1:1000, Cell Signaling #3691) and anti-EIF2K (1:1000, Cell Signaling #3692). Western blots shown in the manuscript are representative experiments of two individual replicates or three individual replicates for puromycin uptake assays. Western blots were quantified using ImageJ software (National Institutes of Health, USA). Densitometric analysis was performed to measure band intensities, and values were normalized as follows: puromycin incorporation blots and total protein levels were normalized to loading controls VINCULIN or ACTIN, while phospho-proteins or methylated proteins were normalized to their respective total protein levels. Where relative levels are reported, the values were further normalized to the control condition.

Expression analysis of HMGA2 in various published datasets

Expression of HMGA2 was quantified using a cohort of resectable ($n = 177$) and metastatic ($n = 253$) patients from Chan-Seng-Yue et al., 2020 and Perera et al., 2022^{51,94}. RNA-seq was performed on frozen laser capture microdissected tumors on the Illumina platform. Reads were aligned using STAR (v.2.7.4a) to human reference genome (hg38; Ensemble v100). Gene expression was calculated in transcripts per million reads mapped using stringtie (v2.0.6). Tumor molecular subtype (Moffitt and Collisson) was inferred using a single sample classifier based on the initial genes published by Moffitt et al., 2015 and Collisson et al., 2011^{54,95}. Expression of HMGA2 was also evaluated at single-cell resolution in a cohort of metastatic ($n = 21$) PDAC patient samples and a patient-derived organoid model exposed to TGF- β from Raghavan et al., 2021⁵³. For the human PDAC organoid experiment, cells were cultured in reduced organoid media (Advanced DMEM/F12, 10 mM HEPES, 1 \times GlutaMAX, 50 ng/mL mEGF, 100 ng/mL hFGF10, 10 nM hGastrin 1, 1.25 mM N-acetylcysteine, 10 mM Nicotinamide, 1 \times B27 supplement, 100 U/mL penicillin/streptomycin, and 1 \times Primocin) and exposed to TGF- β 1 for different durations (38 or 73 days) before harvesting⁵³. As previously described⁵³, single-cell suspensions from tumor or organoid samples were processed following the Seq-Well protocol^{96,97}, sequenced on the Illumina platform, and reads were aligned to the human reference genome (hg19). Each sample's digital gene expression matrix (DGE, cells \times genes) was trimmed for low quality cells, doublets, and genes that were not detected in at least 50

cells. UMI count data was divided by total transcripts captured on a per cell basis and multiplied by a scaling factor of 10,000 to normalize values, followed by natural log transformation for downstream analysis. Expression scores were computed as previously described^{53,98} for basal and classical PDAC molecular subtypes using genes published by Moffitt et al., 2015⁹⁵. KRT5 and KRT81 expression was not captured in the patient-derived organoid model.

Polysome fractionations

KP4 cells were cultured and transfected with either non-targeting or HMGA2-targeting siRNA as described in Supplementary Materials and Methods. Cells were harvested by trypsinization, collected in media and centrifuged. The resulting cell pellets were resuspended in 1 mL of a 0.10 mg/mL stock of cycloheximide in PBS. The cell suspension was incubated on ice for 10 min, centrifuged, and the resulting pellet was snap frozen in liquid nitrogen before storage at -80°C . Frozen cell pellets were lysed in 150 μL polysome lysis buffer (10 mM Tris-HCl pH 7.4 [Ambion, AM9851 (pH 7.0) and AM9856 (pH 8.0)], 132 mM NaCl (Ambion, AM9760G), 1.4 mM MgCl₂ (Ambion, AM9530G), 19 mM DTT (Sigma, 43815), 142 $\mu\text{g/mL}$ cycloheximide (Sigma, C7698), 0.1% Triton X-100 (Fisher, BP151), 0.2% NP-40 (Pierce, PI28324), 607 U/mL SUPERase-In RNase Inhibitor (Life Technologies, AM2696) for 45 min on ice, and vortexed every 10 min. Lysates were centrifuged at $9300 \times g$ for 5 min at 4°C to pellet cell debris, and the supernatants were transferred into fresh tubes. A portion of each lysate (15 μL) was reserved as the total RNA input sample and the remaining volume was layered onto 10–30% (w/v) linear sucrose gradients for ribosome fractionation (gradients prepared in Seton 7030 ultracentrifuge tubes). The gradients were centrifuged at $287,472.3 \times g$ for 3 h at 4°C in a Beckman SW41Ti rotor. Fractions (400 μL each) were collected by upward displacement into collection tubes (Gilson Fraction Collector) through a Bio-Rad EMI UV monitor (Bio-Rad) for continuous measurement of the absorbance at 254 nm using a Biocomp Gradient Station (Biocomp).

Real-Time RT-PCR Analysis

Total RNA was extracted using RNeasy Mini Kit (Qiagen, #74106) as described by the manufacturer. For cDNA synthesis, 1 μg of total RNA was reverse-transcribed using the QuantiTect Reverse Transcription Kit (Qiagen, #205313). Real-time PCR was run in duplicates using iTaq(tm) Universal SYBR(R) Green Supermix (Biorad), following the manufacturer's instructions, with the exception that the final volume was 12.5 μL of SYBR green reaction mix. Real-time monitoring of PCR amplification was performed using the CFX384 Real-Time system (Biorad). Data were expressed as mRNA levels normalized to the *ACTB* expression level in each sample and are represented as mean \pm s.e.m. between three independent experiments unless otherwise indicated in the figure legend. The primer sequences are listed in Table S3. Small RNAs were extracted using miRNeasy Kit (Fisher, # 217004). Quantitative TaqMan microRNA assays were performed according to the manufacturer's instructions, using primers and probes that specifically detect mature Mirlet7d (ThermoFisher Scientific #4427975 ID 002283), Mirlet7a (ThermoFisher Scientific #4427975 ID 000377), Mirlet7f (ThermoFisher Scientific #4427975 ID 000382) and U6 control (ThermoFisher Scientific #4427975 ID 001973).

Cell line xenografts

All mouse procedures were conducted in accordance with the Fred Hutchinson Cancer Center IACUC guidelines. Xenografts were performed in 6–8 week-old NSG mice of both sexes. Typically, $0.5\text{--}2 \times 10^6$ cells in 200 μL suspension of 50% Matrigel (Corning) in DPBS were injected into each flank of the mouse. Caliper measurements of tumors were recorded three times per week. For orthotopic injections, a small left-flank incision was made to expose the pancreas. Typically, 0.5×10^6 of engineered Capan-2 cells or 0.1×10^6 of human organoids in

30 μ L suspension of 50% Matrigel (Corning) in DPBS were injected into the pancreas. Mice were euthanized if they met one or more predefined criteria, including tumor ulceration or necrosis, tumor bleeding or infection, impaired mobility, inability to access food or water, or significant interference with vital physiological functions (e.g., respiration, swallowing, or excretion). For cell line xenografts, tumor burden was closely monitored, with euthanasia required if tumors exceeded the maximal size permitted by institutional guidelines. Tumor size limitations depended on position, overall animal health, and the ability to move, eat, and drink normally. The maximum permitted tumor size was: 2 cm average diameter (unilateral) or 1.5 cm average diameter (bilateral) per tumor. For HMGA2-overexpressing xenografts, mice were fed with 200 μ g/ml doxycycline in their drinking water a week prior before implantation.

Patient-derived xenografts

PDX models were acquired from the NCI PDMR (292921-168-R) and JAX PDX models (TM01212). Vials of cryopreserved PDX tissue fragments were revived and subsequently repassaged as fresh whole tissue into female NSG (NOD scid gamma) mice. Freshly harvested tissue was then used for implantation of study cohorts of female nude mice (#002019, JAX). Every PDX model tested negative for human pathogens (IDEXX h-IMPACT panel). An aseptic standardized procedure was used uniformly: \sim 1–2 mm³ PDX tissue chunks (37 °C) were rinsed in RPMI, suspended in Matrigel (Corning), and implanted subcutaneously into the right flanks of 6–8 week-old nude female mice under isoflurane anesthesia. Preemptive analgesia was provided using buprenorphine SR (0.05 mg/kg). Post-surgically, tumor growth and body condition were monitored, and tumors were measured with electronic calipers. When average tumor diameters of 3–5 mm³ were reached, mice were treated twice daily by oral gavage with vehicle or HHT (0.5 mg/kg; FH15974, Bioosynth) diluted in DPBS for 21 days. Caliper measurements of tumors and body weights were recorded three times per week. For survival studies, mice with severe weight loss or average tumor diameters of 20 mm were used as endpoint.

Proliferation IC50 Assay

Cells were plated in 96-well plates (1000 cells/well) in culture medium. The following day, increasing doses of either HHT or DMSO control (S9015; Selleckchem) were added, and the cells were allowed to grow until DMSO-treated wells reached confluency (5–7 days). To quantify viable cells, MTT (M-6494; ThermoFisher Scientific) was added to the culture media at a final concentration of 1 mg/mL and incubated for 3 h at 37 °C. Formazan crystals were solubilized with 100 μ L/well of DMSO and absorbance was read at 490 nm and normalized to DMSO control. MTT proliferation assays were performed in five replicates. Individual IC50s were calculated using GraphPad Prism. The relative IC50 was determined by dividing the individual IC50s by the average IC50 of empty control.

Histology

Murine pancreata were harvested, fixed for 2 days in 10% buffered formaldehyde, then paraffin embedded and sectioned (5 μ m thickness) by the Fred Hutchinson Cancer Center Experimental Histopathology Core. Hematoxylin and eosin staining was performed using standard methods. For quantification of PanINs, total percentage of PDA/high-grade PanINs, low-grade PanINs, and normal ducts were quantified per section in a blinded fashion by pathologist (A.N.S.). A.N.S. also took representative images of 5, 10, 15, and 30-week-old, endpoint, and doxycycline withdrawal K28C and KC pancreata. Primary antibodies used were as follows: anti-FLAG (Sigma #F1804) 1:1000, anti-Lin28B (LS Bio, #LS-B3423) 1:400, anti-HMGA2 (CST #5269) 1:100, anti-p53 (Vector VP-P956) 1:400, anti-GATA6 (CST #5851S) 1:100, and anti-phospho-S6K (Abcam # ab2571) 1:100 for human tissues. Stained slides were photographed with a Nikon Eclipse Ni-U microscope.

Immunohistochemistry was scored semi quantitatively, in a blinded fashion (N.Y.). HMGA2 was scored on a 0 (no staining) to 3 (strongest intensity) scale in tumor epithelial cells. pS6K T389 and HMGA2 were scored as percentage intensity of tumor epithelial cells at three randomly selected locations per sample.

Immunofluorescence

FFPE tissue slices were stained by immunofluorescence as previously described⁹⁹, with some modifications. Antigen retrieval was performed with 10 mM trisodium citrate dihydrate buffer pH 6.0 and samples were boiled at 95 °C for 20 min. Blocking was performed with 5% normal goat serum and 1% BSA in permeabilization solution (PBS 1x/gelatin (0.2% w/v)/Triton (0.25% v/v)). Primary antibodies (KRT5, Abcam #ab52635; KRT17, Thermo Fisher #MA1-06325 and KRT81, SantaCruz #sc-100929) were diluted 1:100 in blocking buffer and samples probed overnight. Secondary antibodies (anti-rabbit 488 (Fisher PISA510038), anti-mouse 555 (Fisher NBP151898)) were used at 1:400, and slides were mounted with mounting media containing DAPI (Vectashield, Vector Laboratories). Pancreatic islets stain strongly positive for KRT5 and were excluded from analyses. KRT5, KRT17 and KRT81 were scored as percentage intensity of tumor epithelial cells at three randomly selected locations per sample.

Multiplex immunohistochemistry

5 μ m sections of primary tumor were sectioned onto positively charged slides and baked for 1 h at 65 °C. Slides were then dewaxed and stained on a Leica BOND RX stainer (Leica, Buffalo Grove, IL) using Leica BOND reagents for dewaxing (Dewax Solution), antigen retrieval and antibody stripping (Epitope Retrieval Solution 2) and rinsing (Bond Wash Solution). Antigen retrieval and antibody stripping was performed at 100 °C, while all other steps were performed at room temperature. Endogenous peroxidase was blocked with 3% H₂O₂ for 5 min, followed by protein blocking with TCT buffer (0.05 M Tris, 0.15 M NaCl, 0.25% Casein, 0.1% Tween, 0.05% ProClin300, pH 7.6) for 10 min. First primary antibody (FAP, ab53066, Abcam) was applied for 1 h, followed by the first secondary antibody for 20 min, then the tertiary TSA-amplification reagent (Akoya Biosciences OPAL fluorophores) for 20 min. A high-stringency wash was performed using high-salt TBST solution (0.05 M Tris, 0.3 M NaCl, 0.1% Tween-20, pH 7.2–7.6). Host-specific polymer HRP was used for all secondary applications, either 1X Opal Anti-Ms + Rb HRP (Akoya Biosciences, Cat #ARH1001EA) or PowerVision Poly-HRP anti-mouse IgG (Leica Biosystems, Cat #PV6114). Primary and secondary antibodies were stripped with retrieval solution for 20 min. The process was then repeated with the second position primary (HMGA2, 5269, Cell Signaling Technology) and secondary antibodies from the 3% H₂O₂ step. The process was continued until all six markers were probed (Third position: KRT17 (EP1623, Abcam), fifth position: KRT5 (XM26, Leica)). For the sixth position (GATA-6 (D61E4, Cell Signaling Technology)), following secondary antibody incubation, Opal TSA-DIG (PerkinElmer Cat #NEL748001KT) was applied for 20 min, followed by a 20 min stripping step in retrieval solution. After this final stripping step, Opal 780 fluor was applied for one hour. High-stringency washes were performed after the secondary, TSA-DIG, and Opal 780 incubation steps. Slides were removed from the autostainer and stained with 5 μ g/mL DAPI (Sigma, Cat #D8417), rinsed, and coverslipped with Prolong Gold Antifade reagent (Invitrogen/Life Technologies, Cat #P36930). Slides were cured at room temperature.

Statistics and Reproducibility

Statistical significance was determined by specific tests and is presented as means \pm SEM as indicated in the figure legends. Statistical analyses were performed using GraphPad Prism v10.4.0. Student's two-tailed or one-tailed *t* test was used when comparing data from two

groups: $*P \leq 0.05$; $**P \leq 0.01$, $***P \leq 0.001$, and $****P \leq 0.0001$. A log-rank test was used to determine significance for Kaplan-Meier analyses. For RNA-seq data, a Wilcoxon Rank sum test or Kruskal-Wallis test was applied. In Supplementary Fig. 1e, P values were determined using Fisher's exact test. Western blots presented are representative. For blots containing multiple cell lines, experiments were repeated twice, while blots with one or two cell lines were repeated three times. Puromycin uptake assays were repeated three times.

Reporting summary

Further information on research design is available in the Nature Portfolio Reporting Summary linked to this article.

Data availability

Newly generated cell lines and organoids can be provided upon request. The data generated in this study are provided in the Supplementary Information/Source Data file. Source data are provided with this paper.

References

- Rahib, L. et al. Projecting cancer incidence and deaths to 2030: the unexpected burden of thyroid, liver, and pancreas cancers in the United States. *Cancer Res.* **74**, 2913–2921 (2014).
- Ducreux, M. et al. Cancer of the pancreas: ESMO clinical practice guidelines for diagnosis, treatment and follow-up. *Ann. Oncol.* **26**, v56–v68 (2015).
- Braxton, A. M. et al. 3D genomic mapping reveals multifocality of human pancreatic precancers. *Nature* **629**, 679–687 (2024).
- Collisson, E. A., Bailey, P., Chang, D. K. & Biankin, A. V. Molecular subtypes of pancreatic cancer. *Nat. Rev. Gastroenterol. Hepatol.* **16**, 207–220 (2019).
- Moss, E. G. & Tang, L. Conservation of the heterochronic regulator Lin-28, its developmental expression and microRNA complementary sites. *Dev. Biol.* **258**, 432–442 (2003).
- Kastenberger, Z. J. & Odorico, J. S. Alternative sources of pluripotency: science, ethics, and stem cells. *Transpl. Rev.* **22**, 215–222 (2008).
- Hanna, J. et al. Direct cell reprogramming is a stochastic process amenable to acceleration. *Nature* **462**, 595–601 (2009).
- Pasquinelli, A. E. et al. Conservation of the sequence and temporal expression of let-7 heterochronic regulatory RNA. *Nature* **408**, 86–89 (2000).
- Heo, I. et al. Lin28 mediates the terminal uridylation of let-7 precursor MicroRNA. *Mol. Cell* **32**, 276–284 (2008).
- Newman, M. A., Thomson, J. M. & Hammond, S. M. Lin-28 interaction with the Let-7 precursor loop mediates regulated microRNA processing. *RNA* **14**, 1539–1549 (2008).
- Viswanathan, S. R., Daley, G. Q. & Gregory, R. I. Selective blockade of microRNA processing by Lin28. *Science* **320**, 97–100 (2008).
- Rybak, A. et al. A feedback loop comprising lin-28 and let-7 controls pre-let-7 maturation during neural stem-cell commitment. *Nat. Cell Biol.* **10**, 987–993 (2008).
- Piskounova, E. et al. Lin28A and Lin28B inhibit let-7 microRNA biogenesis by distinct mechanisms. *Cell* **147**, 1066–1079 (2011).
- Yang, D. H. & Moss, E. G. Temporally regulated expression of Lin-28 in diverse tissues of the developing mouse. *Gene Expr. Patterns* **3**, 719–726 (2003).
- Büssing, I., Slack, F. J. & Grosshans, H. let-7 microRNAs in development, stem cells and cancer. *Trends Mol. Med.* **14**, 400–409 (2008).
- Johnson, S. M. et al. RAS is regulated by the let-7 microRNA family. *Cell* **120**, 635–647 (2005).
- Mayr, C., Hemann, M. T. & Bartel, D. P. Disrupting the pairing between let-7 and Hmga2 enhances oncogenic transformation. *Science* **315**, 1576–1579 (2007).
- Sampson, V. B. et al. MicroRNA let-7a down-regulates MYC and reverts MYC-induced growth in Burkitt lymphoma cells. *Cancer Res.* **67**, 9762–9770 (2007).
- Thornton, J. E. & Gregory, R. I. How does Lin28 let-7 control development and disease? *Trends Cell Biol.* **22**, 474–482 (2012).
- Viswanathan, S. R. et al. Lin28 promotes transformation and is associated with advanced human malignancies. *Nat. Genet.* **41**, 843–848 (2009).
- Iliopoulos, D., Hirsch, H. A. & Struhl, K. An epigenetic switch involving NF- κ B, Lin28, Let-7 MicroRNA, and IL6 links inflammation to cell transformation. *Cell* **139**, 693–706 (2009).
- Kugel, S. et al. SIRT6 suppresses pancreatic cancer through control of Lin28b. *Cell* **165**, 1401–1415 (2016).
- King, C. E. et al. LIN28B promotes colon cancer progression and metastasis. *Cancer Res.* **71**, 4260–4268 (2011).
- Lu, L. et al. Pluripotent factor lin-28 and its homologue lin-28b in epithelial ovarian cancer and their associations with disease outcomes and expression of let-7a and IGF-II. *Eur. J. Cancer* **45**, 2212–2218 (2009).
- Boyerinas, B. et al. Identification of let-7-regulated oncofetal genes. *Cancer Res.* **68**, 2587–2591 (2008).
- Nguyen, L. H. et al. Lin28b is sufficient to drive liver cancer and necessary for its maintenance in murine models. *Cancer Cell* **26**, 248–261 (2014).
- Poleskaya, A. et al. Lin-28 binds IGF-2 mRNA and participates in skeletal myogenesis by increasing translation efficiency. *Genes Dev.* **21**, 1125–1138 (2007).
- Yantiss, R. K. et al. KOC (K homology domain containing protein overexpressed in cancer): a novel molecular marker that distinguishes between benign and malignant lesions of the pancreas. *Am. J. Surg. Pathol.* **29**, 188–195 (2005).
- Thakur, A., Bollig, A., Wu, J. & Liao, D. J. Gene expression profiles in primary pancreatic tumors and metastatic lesions of Ela-c-myc transgenic mice. *Mol. Cancer* **7**, 11 (2008).
- Franses, J. W. et al. Pancreatic circulating tumor cell profiling identifies LIN28B as a metastasis driver and drug target. *Nat. Commun.* **11**, 3303 (2020).
- Zhu, H. et al. The Lin28/let-7 axis regulates glucose metabolism. *Cell* **147**, 81–94 (2011).
- Bardeesy, N. et al. Both p16(Ink4a) and the p19(Arf)-p53 pathway constrain progression of pancreatic adenocarcinoma in the mouse. *Proc. Natl. Acad. Sci. USA* **103**, 5947–5952 (2006).
- Hingorani, S. R. et al. Trp53R172H and KrasG12D cooperate to promote chromosomal instability and widely metastatic pancreatic ductal adenocarcinoma in mice. *Cancer Cell* **7**, 469–483 (2005).
- Adsay, V., Logani, S., Sarkar, F., Crissman, J. & Vaitkevicius, V. Foamy gland pattern of pancreatic ductal adenocarcinoma: a deceptively benign-appearing variant. *Am. J. Surg. Pathol.* **24**, 493–504 (2000).
- Bagci, P. et al. Large duct type invasive adenocarcinoma of the pancreas with microcystic and papillary patterns: a potential microscopic mimic of non-invasive ductal neoplasia. *Mod. Pathol.* **25**, 439–448 (2012).
- Biankin, A. V. et al. Pancreatic cancer genomes reveal aberrations in axon guidance pathway genes. *Nature* **491**, 399–405 (2012).
- Katarina, R. K., Oshima, M. & Motomizu, S. On-line collection/concentration and determination of transition and rare-earth metals in water samples using multi-auto-pret system coupled with inductively coupled plasma-atomic emission spectrometry. *Talanta* **78**, 1043–1050 (2009).
- Pei, H. et al. FKBP51 affects cancer cell response to chemotherapy by negatively regulating Akt. *Cancer Cell* **16**, 259–266 (2009).
- Pérez-Mancera, P. A. et al. The deubiquitinase USP9X suppresses pancreatic ductal adenocarcinoma. *Nature* **486**, 266–270 (2012).

40. Zhang, G. et al. DPEP1 inhibits tumor cell invasiveness, enhances chemosensitivity and predicts clinical outcome in pancreatic ductal adenocarcinoma. *PLoS One* **7**, e31507 (2012).
41. Barretina, J. et al. The cancer cell line encyclopedia enables predictive modelling of anticancer drug sensitivity. *Nature* **483**, 603–607 (2012).
42. Mansoori, B. et al. HMGA2 as a critical regulator in cancer development. *Genes* **12**, 269 (2021).
43. Noro, B. et al. Molecular dissection of the architectural transcription factor HMGA2. *Biochemistry* **42**, 4569–4577 (2003).
44. Tessari, M. A. et al. Transcriptional activation of the cyclin A gene by the architectural transcription factor HMGA2. *Mol. Cell Biol.* **23**, 9104–9116 (2003).
45. Ozturk, N., Singh, I., Mehta, A., Braun, T. & Barreto, G. HMGA proteins as modulators of chromatin structure during transcriptional activation. *Front Cell Dev. Biol.* **2**, 5 (2014).
46. Fusco, A. & Fedele, M. Roles of HMGA proteins in cancer. *Nat. Rev. Cancer* **7**, 899–910 (2007).
47. Sgarra, R. et al. Nuclear phosphoproteins HMGA and their relationship with chromatin structure and cancer. *FEBS Lett.* **574**, 1–8 (2004).
48. Thuault, S. et al. Transforming growth factor-beta employs HMGA2 to elicit epithelial-mesenchymal transition. *J. Cell Biol.* **174**, 175–183 (2006).
49. Dobersch, S. et al. Positioning of nucleosomes containing γ -H2AX precedes active DNA demethylation and transcription initiation. *Nat. Commun.* **12**, 1072 (2021).
50. Chiou, S. H. et al. Hmga2 is dispensable for pancreatic cancer development, metastasis, and therapy resistance. *Sci. Rep.* **8**, 14008 (2018).
51. Chan-Seng-Yue, M. et al. Transcription phenotypes of pancreatic cancer are driven by genomic events during tumor evolution. *Nat. Genet.* **52**, 231–240 (2020).
52. Aung, K. L. et al. Genomics-Driven Precision Medicine for Advanced Pancreatic Cancer: Early Results from the COMPASS Trial. *Clin. Cancer Res.* **24**, 1344–1354 (2018).
53. Raghavan, S. et al. Microenvironment drives cell state, plasticity, and drug response in pancreatic cancer. *Cell* **184**, 6119–6137 (2021).
54. Collisson, E. A. et al. Subtypes of pancreatic ductal adenocarcinoma and their differing responses to therapy. *Nat. Med.* **17**, 500–503 (2011).
55. Bozóky, B. et al. Stabilization of the classical phenotype upon integration of pancreatic cancer cells into the duodenal epithelium. *Neoplasia* **23**, 1300–1306 (2021).
56. Roa-Peña, L. et al. Keratin 17 identifies the most lethal molecular subtype of pancreatic cancer. *Sci. Rep.* **9**, 11239 (2019).
57. Williams, H. L. et al. Spatially resolved single-cell assessment of pancreatic cancer expression subtypes reveals co-expressor phenotypes and extensive intratumoral heterogeneity. *Cancer Res.* **83**, 441–455 (2023).
58. Muckenhuber, A. et al. Pancreatic ductal adenocarcinoma subtyping using the biomarkers hepatocyte nuclear factor-1A and cytokeratin-81 correlates with outcome and treatment response. *Clin. Cancer Res.* **24**, 351–359 (2018).
59. Werba, G. et al. Single-cell RNA sequencing reveals the effects of chemotherapy on human pancreatic adenocarcinoma and its tumor microenvironment. *Nat. Commun.* **14**, 797 (2023).
60. O’Kane, G. M. et al. GATA6 expression distinguishes classical and basal-like subtypes in advanced pancreatic cancer. *Clin. Cancer Res.* **26**, 4901–4910 (2020).
61. de Andrés, M. P. et al. GATA4 and GATA6 loss-of-expression is associated with extinction of the classical programme and poor outcome in pancreatic ductal adenocarcinoma. *Gut* **72**, 535–548 (2023).
62. Duan, K. et al. The value of GATA6 immunohistochemistry and computer-assisted diagnosis to predict clinical outcome in advanced pancreatic cancer. *Sci. Rep.* **11**, 14951 (2021).
63. Hsieh, A. C. et al. The translational landscape of mTOR signalling steers cancer initiation and metastasis. *Nature* **485**, 55–61 (2012).
64. Hsieh, A. C. et al. Genetic dissection of the oncogenic mTOR pathway reveals druggable addiction to translational control via 4EBP-eIF4E. *Cancer Cell* **17**, 249–261 (2010).
65. Robichaud, N., Sonenberg, N., Ruggero, D. & Schneider, R. J. Translational control in cancer. *Cold Spring Harb. Perspect Biol.* **11**, 254–266 (2019).
66. Missios, P. et al. LIN28B alters ribosomal dynamics to promote metastasis in MYCN-driven malignancy. *J Clin Invest* **131**, e145142 (2021).
67. Luk, I. S. et al. SRC inhibition enables formation of a growth suppressive MAG1-PP2A complex in isocitrate dehydrogenase-mutant cholangiocarcinoma. *Sci. Transl. Med.* **16**, ead7685 (2024).
68. Hahn, K. et al. PP2A regulatory subunit PP2A-B’ counteracts S6K phosphorylation. *Cell Metab.* **11**, 438–444 (2010).
69. Fowle, H., Zhao, Z. & Grana, X. PP2A holoenzymes, substrate specificity driving cellular functions and deregulation in cancer. *Adv. Cancer Res.* **144**, 55–93 (2019).
70. Janssens, V., Longin, S. & Goris, J. PP2A holoenzyme assembly: in cauda venenum (the sting is in the tail). *Trends Biochem. Sci.* **33**, 113–121 (2008).
71. Rasool, R. U. et al. Loss of LCMT1 and biased protein phosphatase 2A heterotrimerization drive prostate cancer progression and therapy resistance. *Nat. Commun.* **14**, 5253 (2023).
72. Leonard, D. et al. Selective PP2A enhancement through biased heterotrimer stabilization. *Cell* **181**, 688–701.e616 (2020).
73. Jana, S. et al. Transcriptional-translational conflict is a barrier to cellular transformation and cancer progression. *Cancer Cell* **41**, 853–870 (2023).
74. Gundlach, J. P. et al. Prognostic significance of high mobility group A2 (HMGA2) in pancreatic ductal adenocarcinoma: malignant functions of cytoplasmic HMGA2 expression. *J. Cancer Res. Clin. Oncol.* **147**, 3313–3324 (2021).
75. Strell, C. et al. Stroma-regulated HMGA2 is an independent prognostic marker in PDAC and AAC. *Br. J. Cancer* **117**, 65–77 (2017).
76. Hristov, A. C. et al. HMGA2 protein expression correlates with lymph node metastasis and increased tumor grade in pancreatic ductal adenocarcinoma. *Mod. Pathol.* **22**, 43–49 (2009).
77. Xiao, G., Wang, X. & Yu, Y. CXCR4/Let-7a axis regulates metastasis and chemoresistance of pancreatic cancer cells through targeting HMGA2. *Cell Physiol. Biochem.* **43**, 840–851 (2017).
78. Flowers, B. M. et al. Cell of origin influences pancreatic cancer subtype. *Cancer Discov.* **11**, 660–677 (2021).
79. Eichhorn, P. J., Creighton, M. P. & Bernards, R. Protein phosphatase 2A regulatory subunits and cancer. *Biochim. Biophys. Acta* **1795**, 1–15 (2009).
80. Welcker, M., Orian, A., Grim, J. E., Eisenman, R. N. & Clurman, B. E. A nucleolar isoform of the Fbw7 ubiquitin ligase regulates c-Myc and cell size. *Curr. Biol.* **14**, 1852–1857 (2004).
81. Westermarck, J. & Hahn, W. C. Multiple pathways regulated by the tumor suppressor PP2A in transformation. *Trends Mol. Med.* **14**, 152–160 (2008).
82. Farrell, A. S. et al. Targeting inhibitors of the tumor suppressor PP2A for the treatment of pancreatic cancer. *Mol. Cancer Res.* **12**, 924–939 (2014).
83. Wang, L. et al. CIP2A expression is associated with altered expression of epithelial-mesenchymal transition markers and predictive of poor prognosis in pancreatic ductal adenocarcinoma. *Tumour Biol.* **34**, 2309–2313 (2013).
84. van Pelt, J. et al. Human pancreatic cancer patients with epithelial-to-mesenchymal transition and an aggressive phenotype show a

- disturbed balance in protein phosphatase type 2A expression and functionality. *J. Transl. Med.* **21**, 317 (2023).
85. Kauko, O. et al. PP2A inhibition is a druggable MEK inhibitor resistance mechanism in KRAS-mutant lung cancer cells. *Sci. Transl. Med.* **10**, eaaq1093 (2018).
 86. Kantarjian, H. M., O'Brien, S. & Cortes, J. Homoharringtonine/omacetaxine mepesuccinate: the long and winding road to food and drug administration approval. *Clin. Lymphoma Myeloma Leuk.* **13**, 530–533 (2013).
 87. Weng, T. Y. et al. Homoharringtonine induced immune alteration for an efficient anti-tumor response in mouse models of non-small cell lung adenocarcinoma expressing Kras mutation. *Sci. Rep.* **8**, 8216 (2018).
 88. Tolcher, A. et al. A phase I trial of LY2584702 tosylate, a p70 S6 kinase inhibitor, in patients with advanced solid tumours. *Eur. J. Cancer* **50**, 867–875 (2014).
 89. Tsimberidou, A. M. et al. Phase 1 study of M2698, a p70S6K/AKT dual inhibitor, in patients with advanced cancer. *J. Hematol. Oncol.* **14**, 127 (2021).
 90. Kawaguchi, Y. et al. The role of the transcriptional regulator Ptf1a in converting intestinal to pancreatic progenitors. *Nat. Genet.* **32**, 128–134 (2002).
 91. Jackson, E. L. et al. Analysis of lung tumor initiation and progression using conditional expression of oncogenic K-ras. *Genes Dev.* **15**, 3243–3248 (2001).
 92. Marino, S., Vooijs, M., van Der Gulden, H., Jonkers, J. & Berns, A. Induction of medulloblastomas in p53-null mutant mice by somatic inactivation of Rb in the external granular layer cells of the cerebellum. *Genes Dev.* **14**, 994–1004 (2000).
 93. Belteki, G. et al. Conditional and inducible transgene expression in mice through the combinatorial use of cre-mediated recombination and tetracycline induction. *Nucleic Acids Res.* **33**, e51 (2005).
 94. Perera, S. et al. hENT1 expression predicts response to gemcitabine and nab-paclitaxel in advanced pancreatic ductal adenocarcinoma. *Clin. Cancer Res.* **28**, 5115–5120 (2022).
 95. Moffitt, R. A. et al. Virtual microdissection identifies distinct tumor and stroma-specific subtypes of pancreatic ductal adenocarcinoma. *Nat. Genet.* **47**, 1168–1178 (2015).
 96. Gierahn, T. M. et al. Seq-Well: portable, low-cost RNA sequencing of single cells at high throughput. *Nat. Methods* **14**, 395–398 (2017).
 97. Hughes, T. K. et al. Second-strand synthesis-based massively parallel scRNA-seq reveals cellular states and molecular features of human inflammatory skin pathologies. *Immunity* **53**, 878–894 (2020).
 98. Tirosh, I. et al. Single-cell RNA-seq supports a developmental hierarchy in human oligodendrogloma. *Nature* **539**, 309–313 (2016).
 99. Zaqout, S., Becker, L. L. & Kaindl, A. M. Immunofluorescence staining of paraffin sections step by step. *Front. Neuroanat.* **14**, 582218 (2020).

Acknowledgements

We thank past and present members of the Kugel laboratory for helpful discussions and Drs. E.O. and G.N. for their support with monoclonal antibodies. Special thanks to M.H. for immunohistochemical stainings and to A.K. and M.R. for their pathological evaluation. This work was supported in part by NIH grants 5R37CA241472-03, 1R01CA255015-01 (to S.K.), R37 CA230617, R01 CA276308, NIH GM135362 (to A.C.H.), and R35 CA231989 (to R.N.E.). Additional support was provided by a Swim Across America Pancreas Cancer Development Research Award (to S.K.), a Walter Benjamin Fellowship (465590102) from the German

Research Foundation, DFG (to S.D.), and a postdoctoral award (PF-24-1196662-01-RMC) from the American Cancer Society (to S.D.). This research was also supported by Comparative Medicine, TRMS, and Experimental Histopathology in Shared Resource of the Fred Hutch/University of Washington Cancer Consortium (P30 CA015704). S.R. is supported by NIH K08 CA260442.

Author contributions

Conception and design: S.D., A.C.H., and S.K. Development of methodology: S.D., N.Y., A.S., and S.K. Acquisition of data: S.D., N.Y., A.S., S.M.C., T.M.R., and C.L.W. Analysis and interpretation of data: S.D., N.Y., A.S., A.N.S., A.Z., G.H.J., A.H.M., S.R., F.N., R.N.E., A.C.H., and S.K. Writing, review, and/or revision of the manuscript: S.D., N.Y., R.N.E., S.H., G.B., G.N., R.N.E., A.C.H., and S.K. Administrative, technical, or material support: S.D., L.P., N.K., B.D., C.L.W., G.N., F.N., and S.K. Study supervision: S.D., A.C.H., and S.K.

Competing interests

S.D., N.Y., and S.K. are inventors on a patent application (provisional) filed by Fred Hutchinson Cancer Center directed for the inventions directed to HMG2's role in PDAC. S.R. receives research funding from Microsoft and holds equity in Amgen outside the described work. The remaining authors declare no competing interests.

Additional information

Supplementary information The online version contains supplementary material available at <https://doi.org/10.1038/s41467-025-60129-1>.

Correspondence and requests for materials should be addressed to Sita Kugel.

Peer review information *Nature Communications* thanks X.G.-A. and the other anonymous reviewer(s) for their contribution to the peer review of this work. A peer review file is available.

Reprints and permissions information is available at <http://www.nature.com/reprints>

Publisher's note Springer Nature remains neutral with regard to jurisdictional claims in published maps and institutional affiliations.

Open Access This article is licensed under a Creative Commons Attribution-NonCommercial-NoDerivatives 4.0 International License, which permits any non-commercial use, sharing, distribution and reproduction in any medium or format, as long as you give appropriate credit to the original author(s) and the source, provide a link to the Creative Commons licence, and indicate if you modified the licensed material. You do not have permission under this licence to share adapted material derived from this article or parts of it. The images or other third party material in this article are included in the article's Creative Commons licence, unless indicated otherwise in a credit line to the material. If material is not included in the article's Creative Commons licence and your intended use is not permitted by statutory regulation or exceeds the permitted use, you will need to obtain permission directly from the copyright holder. To view a copy of this licence, visit <http://creativecommons.org/licenses/by-nc-nd/4.0/>.

© The Author(s) 2025